Field data-based evaluation of methods for recovering surface wave elevation from pressure measurements

A Mouragues, P. Bonneton, D Lannes, B. Castelle, V. Marieu

▶ To cite this version:

HAL Id: hal-02384062
https://hal.science/hal-02384062

Submitted on 28 Nov 2019

Accepted Manuscript

Field data-based evaluation of methods for recovering surface wave elevation from pressure measurements

A. Mouragues, P. Bonneton, D. Lannes, B. Castelle, V. Marieu
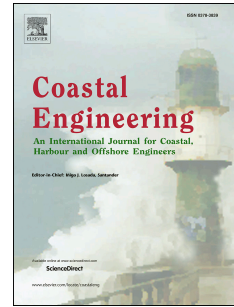
Please cite this article as: Mouragues, A., Bonneton, P., Lannes, D., Castelle, B., Marieu, V., Field data-based evaluation of methods for recovering surface wave elevation from pressure measurements, *Coastal Engineering* (2019), doi: https://doi.org/10.1016/j.coastaleng.2019.04.006.
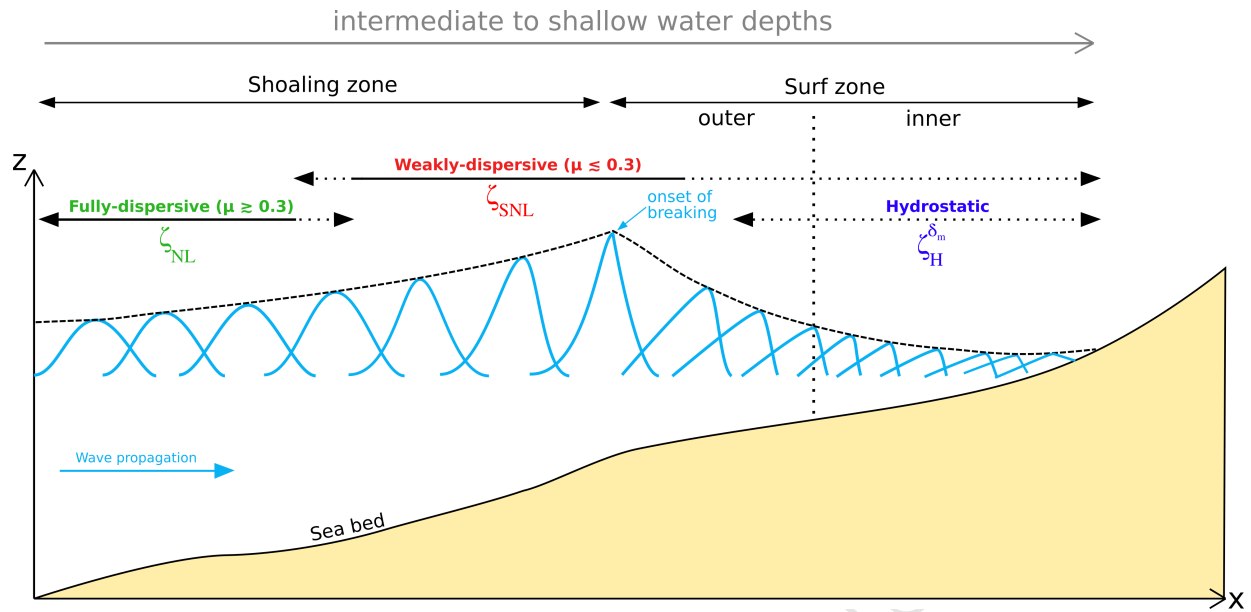
- Methods for recovering surface wave elevation from pressure measurements are evaluated

- Limitations of the commonly-used linear reconstruction methods are highlighted

- The input of recently developed nonlinear reconstruction methods on predicting the largest waves is showcased

Field data-based evaluation of methods for recovering surface wave elevation from pressure measurements

A. Mouragues[a,*], P. Bonneton[a], D. Lannes[b], B. Castelle[a], V. Marieu[a]

[a]*University of Bordeaux; CNRS; UMR 5805 EPOC, Allée Geoffroy Saint-Hilaire, F-33615 Pessac, France*
[b]*University of Bordeaux; IMB and CNRS UMR 5251, F-33405 Talence, France*

Abstract

We compare different methods to reconstruct the surface elevation of irregular waves propagating outside the surf zone from pressure measurements at the bottom. The traditional transfer function method (TFM), based on the linear wave theory, predicts reasonably well the significant wave height but cannot describe the highest frequencies of the wave spectrum. This is why the TFM cannot reproduce the skewed shape of nonlinear waves and strongly underestimates their crest elevation. The surface elevation reconstructed from the TFM is very sensitive to the value of the cutoff frequency. At the individual wave scale, high-frequency tail correction strategies associated with this method do not significantly improve the prediction of the highest waves. Unlike the TFM, the recently developed weakly-dispersive nonlinear reconstruction method correctly reproduces the wave energy over a large number of harmonics leading to an accurate estimation of the peaked and skewed shape of the highest waves. This method is able to recover the most nonlinear waves within wave groups which some can be characterized as extreme waves. It is anticipated that using relevant reconstruction method will improve the description of individual wave transformation close to breaking.

Keywords: wave measurements, pressure sensor, reconstruction methods, Acoustic Surface Tracking, wave-by-wave analysis, nonlinear waves, extreme

---

[*]Corresponding author
Email address: `arthur.mouragues@u-bordeaux.fr` (A. Mouragues)

waves

___

1. Introduction

Pressure sensors have long been used to measure waves in the coastal zone mainly because of their robustness, low-cost aspect and convenience to deploy. However, they do not provide direct measurement of the wave surface elevation.

5 The widely-used method to reconstruct the wave surface elevation from pressure measurements at the bottom is the so-called transfer function method (TFM; e.g. Bishop and Donelan, 1987 [1]), based on the linear wave theory. The TFM allows to recover linear wave fields and gives a reliable estimate of the significant wave height (i.e wave energy). Guza and Thornton (1980) [2] found

10 that the total harmonic variance could be retrieved with error of 7.6 % near the breakpoint. However, for the highest frequencies, the energy density spectra reconstructed from the TFM blows up. To prevent the latter, a cutoff frequency is commonly used (e.g. Lee and Wang, 1984 [3]; Bishop and Donelan, 1987 [1]). Contrary to what is generally accepted in the literature for swell reconstruction,

15 the need for such a cutoff is mainly due to wave nonlinearities rather than to pressure measurement noise (Bonneton and Lannes, 2017 [4]). In this paper, we will show that the cutoff frequency is artificial and that the TFM solution is very sensitive to its value.

In shallow water, nonlinear interactions induce the development of high-frequency

20 harmonics which cannot be correctly reproduced by the TFM. Martins et al., 2017 [5] found that the TFM fails to recover the peaked and skewed shape of nonlinear waves with individual wave height error up to 30 %. However, well predicting nonlinear waves, especially in the shoaling zone, is of paramount importance for many coastal applications. Indeed, the most nonlinear waves are

25 very often found to be the largest waves. An accurate prediction of these waves is then essential for applications involving extreme wave events, wave submersion studies, or coastal construction projects that need to cope with the height of the most extreme waves. Moreover, an accurate characterization of wave

2

skewness and asymmetry is essential for studying sediment transport (Dubarbier et al., 2015 [6]). Lastly, the surface wave reconstruction is also crucial for the calibration of phase-averaged wave model parameters (e.g. Booij et al., 1999 [7]) and for the validation of phase-resolving wave models (e.g. Zijlema et al. 2011 [8], Bonneton et al., 2011 [9]).

In the present paper, we review and apply the main methods designed to reconstruct *in situ* irregular waves. First, we present the commonly-used linear methods as well as recently developed nonlinear methods. Different high-frequency tail correction procedures associated with the TFM are also reviewed. Then, we apply and compare each method with field data, in terms of spectral and temporal parameters, in near-breaking conditions. In such conditions, wave groups contain highly nonlinear waves for which the use of the TFM, based on the linear wave theory, is questionable. More importantly, these waves need to be properly described as they control the break point position and can be characterized as extreme waves. Finally, we conduct a wave-by-wave analysis of the whole dataset in order to compare each method over a large range of nonlinearities.

2. Reconstruction methods

In this section, the main methods to reconstruct irregular wave surface elevation from *in situ* pressure measurements at the bottom are reviewed. We focus on unbroken waves propagating outside the surf zone in intermediate to shallow water depth, for which the flow can be assumed irrotational. In this work, the bottom variation contribution is assumed negligible, which is true for many coastal applications. The background current contribution is also assumed negligible, which is true for most wave-dominated coastal areas far from river mouths or tidal inlets. Bonneton and Lannes (2017) [4] derived a reconstruction formula which takes into account a background current. However, their method requires additional velocity measurement, which, in most nearshore field campaigns, is rarely collected at the same location as the pressure sensor, and is therefore out

3

of scope of the present paper.

Three main length scales are critical to the problem addressed here : the wave
60 amplitude a, the characteristic horizontal length scale L ($k = 1/L$ the typical
wave number) and the mean water depth h_0. The wave propagation is then
controlled by two dimensionless parameters :

$$\epsilon = \frac{a}{h_0}, \qquad \mu = \left(\frac{h_0}{L}\right)^2 = (kh_0)^2, \qquad (1)$$

where ϵ is a nonlinearity parameter and μ is a shallowness (or dispersion) pa-
rameter; or alternatively the steepness parameter σ :

$$\sigma = \frac{a}{L} = \epsilon\sqrt{\mu}. \qquad (2)$$

65 From a practical point of view, deep water cases ($\mu \gg 1$) are disregarded as
pressure measurements are not relevant in such water depths. Reconstruction
methods are usually based on an asymptotic expansion of the irrotationnal wave
equations in terms of the steepness parameter σ, which is a small parameter for
most coastal waves. The small steepness regime encompasses the two following
70 scenarios: large amplitude waves ($\epsilon \sim 1$) in shallow water ($\mu \ll 1$) and small
amplitude waves ($\epsilon \ll 1$) in intermediate depth ($\mu \sim 1$).

For the sake of clarity, a two-dimensional wave field associated with the Carte-
sian coordinates (x,z) is considered, where x corresponds to the horizontal axis
along which waves propagate and z is the positive-upward vertical axis (see
75 Fig. 1). The mean water level and the free surface elevation are defined by
$z = 0$ and $z = \zeta(x,t)$, respectively. The pressure sensor is located at a dis-
tance δ_{m} from the bottom level $z = -h_0$ and provides the measured pressure
$P_m(t) = P(z = -h_0 + \delta_{\mathrm{m}}, t)$.

4
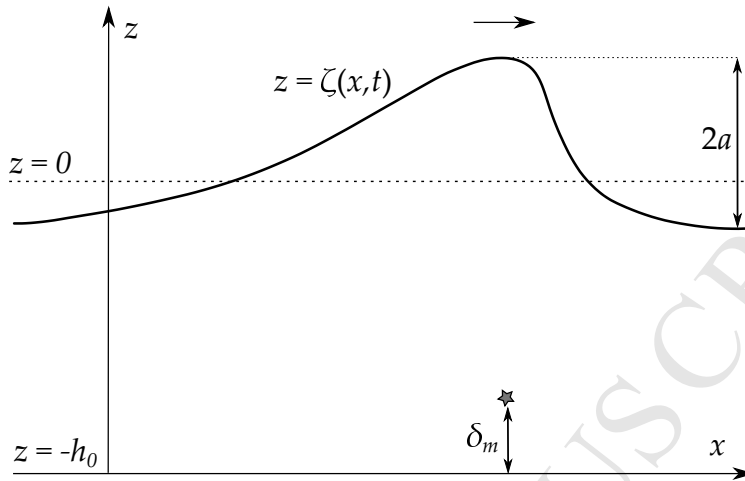
Figure 1: Definition sketch of the physical variables. x and z are the horizontal (wave propagation axis) and vertical axis, respectively. $z = 0$ is the mean water level and $-h_0$ is the constant bottom elevation. $\zeta(x, t)$ is the surface wave elevation, a is the characteristic wave amplitude and δ_m represents the distance from the bottom where the pressure sensor is located.

For very long waves (very small μ), the surface elevation can be estimated from the hydrostatic equilibrium. The hydrostatic reconstructed elevation, $\zeta_H^{\delta_m}$, is then given by :

$$\zeta_H^{\delta_m}(t) = \frac{P_m(t) - P_a}{\rho g} + \delta_m - h_0, \tag{3}$$

where P_a is the constant atmospheric pressure, ρ is the water density and g is the gravity. This hydrostatic reconstruction (Eq. 3) gives good results for tides and tsunamis, but cannot be applied to wind waves which have non-hydrostatic characteristics. Some of the most commonly-used non-hydrostatic linear reconstruction methods are introduced below, and the recently developed nonlinear approaches are further presented.

2.1. Linear methods

2.1.1. Linear wave theory

The derivation of the following reconstruction method can be applied to three-dimensional wave fields but a two-dimensional wave field is considered here for

5

the sake of derivation simplicity (see Fig. 1). The fluid motion is governed by the free-surface incompressible Euler equations. From the irrotational assumption, the horizontal velocity u and the vertical velocity w are given by the velocity

95 potential ϕ as : $u = \partial_x \phi$ and $w = \partial_z \phi$. Neglecting the $O(\sigma)$ terms in the Euler equations, the following linearized system is obtained :

$$\partial_{xx}\phi + \partial_{zz}\phi = 0 \qquad \text{for } z \in [-h_0, 0] \qquad (4)$$

$$\partial_t\phi + \frac{P(z,t) - P_a}{\rho} + gz = 0 \qquad \text{for } z \in [-h_0, 0], \qquad (5)$$

where Eq. 4 is the mass conservation equation and Eq. 5 is the linearized Bernoulli equation. This set of equations is completed by linearized boundary conditions at the bottom and at the surface :

$$\partial_z\phi = 0 \qquad \text{at } z = -h_0 \qquad (6)$$

$$\partial_z\phi = \partial_t\zeta \qquad \text{at } z = 0 \qquad (7)$$

$$P = P_a \qquad \text{at } z = 0. \qquad (8)$$

100 Evaluating Eq. 5 at $z = -h_0 + \delta_{\mathrm{m}}$ and $z = 0$ results in the following expression of $\zeta_H^{\delta_{\mathrm{m}}}$ and ζ :

$$\zeta_H^{\delta_{\mathrm{m}}}(t) = -\frac{1}{g}\partial_t\phi \qquad \text{at } z = -h_0 + \delta_{\mathrm{m}} \qquad (9)$$

$$\zeta(t) = -\frac{1}{g}\partial_t\phi \qquad \text{at } z = 0. \qquad (10)$$

The variables ζ, $\zeta_H^{\delta_{\mathrm{m}}}$ and ϕ are then decomposed using the following Fourier transform in space :

$$\mathcal{F}_X\{f\}(k) = \int_{\mathbb{R}} f(x)e^{-ikx}\,\mathrm{d}x, \qquad (11)$$

where $\mathcal{F}_X\{f\}$ is the Fourier transform in space of the function $f : x \mapsto f(x)$.

6

105 Combining Eq. 4 and 6, we get the expression of the Fourier transform in space of ϕ :

$$\mathcal{F}_X\{\phi\}(k, z, t) = B \cosh(k(z + h_0)), \qquad (12)$$

where B is an independent function of z.

Plugging Eq. 12 into Eq. 9 and 10, ζ can be expressed as a function of $\zeta_H^{\delta_m}$:

$$\mathcal{F}_X\{\zeta\}(k, t) = K_P(k)\mathcal{F}_X\{\zeta_{\mathrm{H}}^{\delta_{\mathrm{m}}}\}(k, t) \qquad (13)$$

$$K_P(k) = \frac{\cosh(kh_0)}{\cosh(k\delta_{\mathrm{m}})}, \qquad (14)$$

where K_P is the non-hydrostatic correction factor.

110 Eq. 13 and 16 are hereafter referred to as the linear formula in space, and the resulting reconstructed surface elevation is hereafter referred to as $\zeta_{\mathrm{L,space}}$ (see linear formula in space in Tab. 1). In Fig. 2, $\zeta_{\mathrm{L,space}}$ is compared to the surface elevation computed from the Full Euler equations (Fenton, 2014 [10]) in case of a periodic weakly nonlinear wave field ($\epsilon = 0.15$ and $\mu = 0.25$). The linear

115 formula in space significantly improves the hydrostatic reconstruction in terms of crest elevation and wave shape, even if the crest elevation is still underestimated compared to the Full Euler solution.

7

Figure 2: Surface elevation of a periodic weakly nonlinear wave, $\epsilon = 0.15$, $\mu = 0.25$, $\delta_{\mathrm{m}} = 0$. Full Euler solution (black line); hydrostatic reconstruction: $\zeta_{\mathrm{H}}^{\delta_{\mathrm{m}}}$ (blue line); linear formula in space: $\zeta_{\mathrm{L,space}}$ (magenta dashed line); see the associated equations in Tab. 1.

2.1.2. Transfer function method

The linear formula (Eq. 13 and 14) involves a Fourier transform in space, which requires the knowledge of $\zeta_{\mathrm{H}}^{\delta_{\mathrm{m}}}$ (or equivalently P_m) over the whole horizontal space. However, for most coastal applications, P_m is only known at one single measurement point. The common practice with the TFM is to replace the Fourier transform in space by a Fourier transform in time, using the linear dispersion relation to express k as a function of the pulsation ω. The TFM writes:

$$\mathcal{F}_T\{\zeta\}(x,\omega) = K_{\mathrm{P}}(\omega)\mathcal{F}_T\{\zeta_{\mathrm{H}}^{\delta_{\mathrm{m}}}\}(x,\omega) \tag{15}$$

$$K_{\mathrm{P}}(\omega) = \frac{\cosh(kh_0)}{\cosh(k\delta_{\mathrm{m}})} \tag{16}$$

$$\omega^2 = gk\tanh(kh_0), \tag{17}$$

8

where the Fourier transform in time is defined by :

$$\mathcal{F}_T\{f\}(\omega) = \int_{\mathbb{R}} f(t)e^{-i\omega t}\,\mathrm{d}t. \tag{18}$$

Bonneton and Lannes (2017) [4] showed that this method is mathematically justified for linear wave fields but is questionable when applied to nonlinear waves. This is illustrated with the periodic weakly nonlinear wave field presented in Fig. 2. The surface elevation computed from the TFM is hereafter referred to as $\zeta_{\mathrm{L,NC}}$ (Eq. 15, 16 and 17; see TFM - no cutoff in Tab. 1). Fig. 3 shows that the energy density of the two first harmonics is well predicted by $\zeta_{\mathrm{L,space}}$ while the energy density of the following harmonics are underestimated.
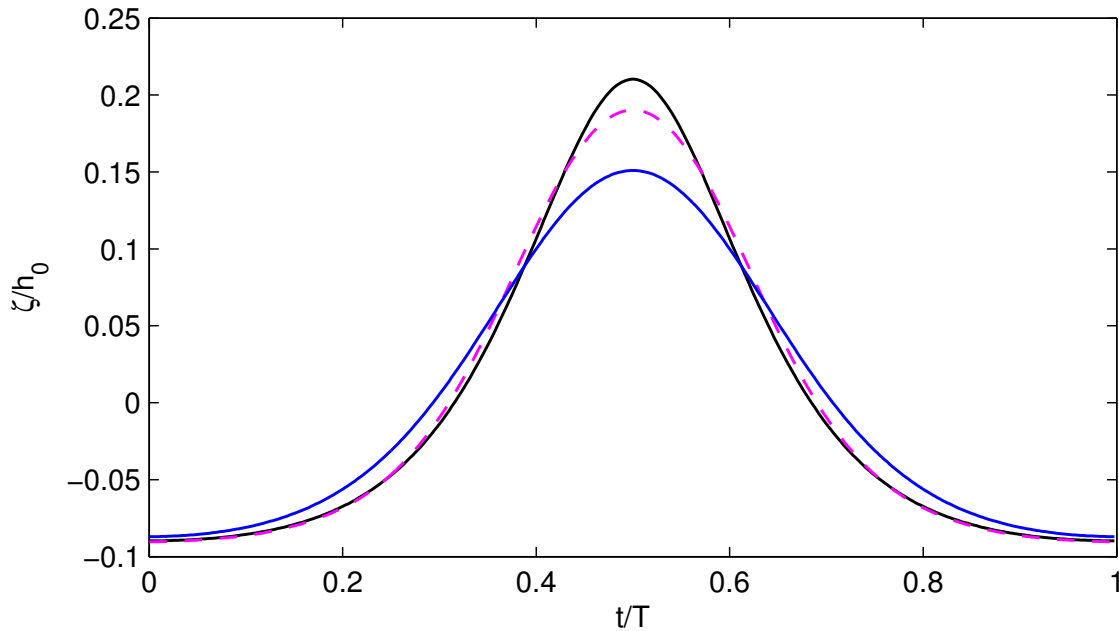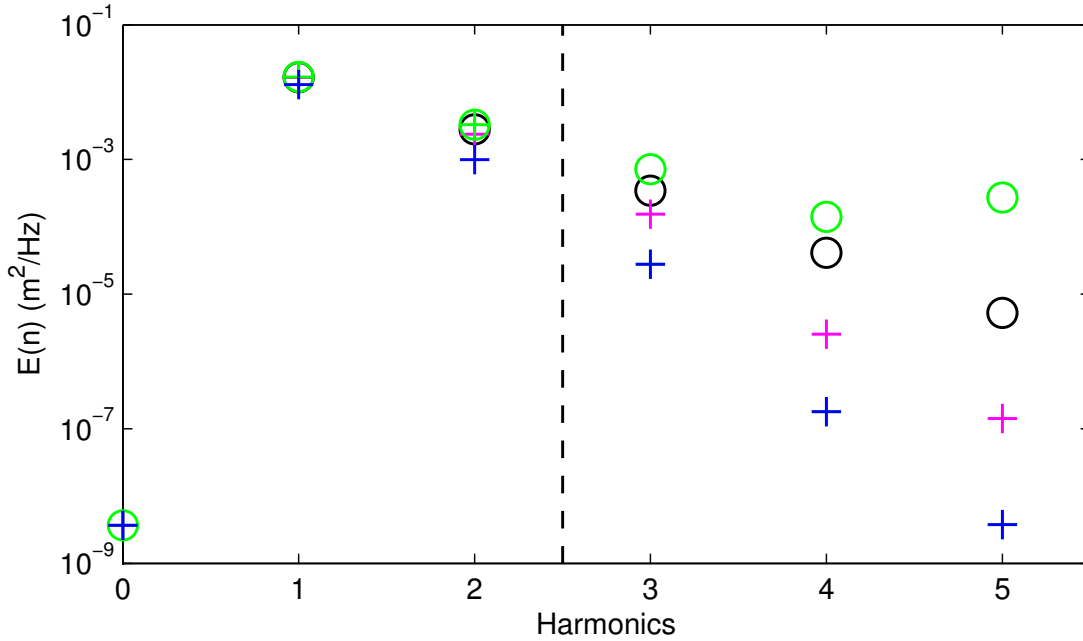

Figure 3: Surface elevation energy density spectra $E(n)$ of a periodic weakly nonlinear wave, $\epsilon = 0.15$, $\mu = 0.25$, $\delta_{\mathrm{m}} = 0$. Full Euler solution (black circle); hydrostatic reconstruction: $\zeta_{\mathrm{H}}^{\delta_{\mathrm{m}}}$ (blue crosses); linear formula in space: $\zeta_{\mathrm{L,space}}$ (magenta crosses); TFM - no cutoff: $\zeta_{\mathrm{L,NC}}$ (green circles); TFM - sharp cutoff: $\zeta_{\mathrm{L,Sh}}$ (green crosses); see the associated equations in Tab. 1. The cutoff harmonic index is indicated by the vertical black dotted line.

Unlike the linear formula in space, the TFM (see $\zeta_{\mathrm{L,NC}}$ in Fig. 3) leads to an

135 energy density overestimation, even for weakly nonlinear waves, which increases rapidly with the harmonics and leads to a blow up of the TFM solution (overestimation of the fifth harmonic by two orders of magnitude). As described by Bonneton et al. (2017) [4], it is due to secondary harmonics which are phase locked, or bound, to the fundamental harmonics and travel at a celerity which

140 is much larger than their intrinsic (linear) phase speed. Thus, the linear dispersive relation (Eq. 17) strongly overestimates the wave number of the harmonics leading to the overestimation of K_P (Eq. 16).

To overcome this TFM problem, the commonly-used approach is to introduce a cutoff frequency f_c. At $f = f_c$, the TFM spectrum is truncated and replaced

145 by the hydrostatic spectrum for $f > f_c$ (equivalent to a low-pass filter). The expression of K_P then becomes:

$$K_P(\omega) = \frac{\cosh(kh_0)}{\cosh(k\delta_m)} \qquad \text{for} \quad \frac{\omega}{2\pi} \leq f_c \qquad (19)$$

$$K_P(\omega) = 1 \qquad \text{for} \quad \frac{\omega}{2\pi} > f_c \qquad (20)$$

Eq. 20 is hereafter referred to as the sharp cutoff and the associated surface elevation is referred to as $\zeta_{L,Sh}$ (see TFM - sharp cutoff in Tab. 1).

It is worth noting that contrary to what is generally accepted in the litera-

150 ture for swell reconstruction, the need for such a cutoff is mainly due to wave nonlinearities rather than to pressure measurement noise. Therefore, f_c can be considered as a nonlinear cutoff frequency. Nonetheless, in most coastal applications, two different empirical approaches are generally used to determine the value of f_c (Smith, 2002 [11]). The first one consists in setting f_c at the

155 frequency where the pressure signal is one order of magnitude higher than the noise floor, which is questionable. In the second approach, f_c is set to the frequency where K_P is less than 10 to 1000, which value depends on the pressure sensor resolution (Wolf, 1997 [12]). The reconstructed wave characteristics are very sensitive to the subjective value of f_c (see Section 4.1.1; Smith, 2002 [11];

160 Jones and Monismith, 2007 [13]). In Fig. 3, the value of f_c is optimized i.e. we set f_c by comparing the wave energy reconstructed by the TFM with no

10

nonlinear cutoff frequency, $\zeta_{\mathrm{L,NC}}$ (see TFM - no cutoff in Tab. 1), and the true wave energy. f_c is taken at the frequency where $\zeta_{\mathrm{L,NC}}$ starts to overestimate the true wave energy (i.e. where K_{P} is too high), here after the second harmonic
165 (see the vertical dashed line in Fig. 3).

In most studies, the direct measurement of the surface wave elevation is not available but is retrieved from pressure measurements and f_c cannot be optimized objectively. Most of the time, it is not clear how the cutoff frequency has been set and, for field applications, its value typically ranges between 0.25
170 and 0.6 Hz (e.g. Guza and Thornton, 1980 [2]; Ruessink et al, 1998 [14]; Smith, 2002 [11]; Sénéchal et al, 2004 [15]). However, the way f_c is set is crucial and can strongly affect the wave shape. Indeed, the cutoff induces spectral information loss beyond f_c that will generate oscillations within the reconstructed time series (see Section 4.1.1). The frequency of these oscillations being of the
175 same order as f_c, those are then strongly dependent on the cutoff and are not physical. This kind of oscillations is hereafter referred to as parasite oscillations.

High-frequency tail empirical correction

As introduced above, the widely-used TFM requires a cutoff frequency. Using the sharp cutoff method (Eq. 20; see TFM - sharp cutoff in Tab. 1) will induce
180 spectral information loss for $f > f_c$ (see Fig. 3). To limit this loss of information, several empirical formula were derived to artificially fill the high-frequency tail. Three empirical methods are presented here.

A first method is to replace the high-frequency tail by a Jonswap diagnostic tail. The energy density spectra $E(f)$ is expressed as a function of f^{-n} where
185 n represents the tail's slope (Eq. 21; see TFM - Jonswap in Tab. 1) :

$$E(f > f_c) = E(f_c) \left(\frac{f}{f_c} \right)^{-n} . \tag{21}$$

The value of n depends on the water depth. $n = 5$ is usually set in deep water while $n = 4$ and $n = 3$ are set for intermediate water and shallow water, respectively.

11

Eq. 21 allows to better predict spectral wave parameters (e.g. Wolf, 1997 [12];

Smith, 2002 [11]; Jones and Monismith, 2007 [13]). However, this method is not able to recover surface elevation time series as the phase signal is not given by this approach.

The two other methods consist in tuning the value of K_{P} beyond f_{c}. Neumeier [16] uses an empirical correction factor $K_{\mathrm{P,L}}$ which linearly decreases over an artificial frequency range (Eq. 22 and 23; see TFM - linear cutoff in Tab. 1).

$$K_{\mathrm{P}}(\omega) = K_{\mathrm{P,L}} \qquad \text{for } f_{\mathrm{c}} < \frac{\omega}{2\pi} < f_{\mathrm{lin}} \qquad (22)$$

$$K_{\mathrm{P}}(\omega) = 1 \qquad \text{for } \frac{\omega}{2\pi} > f_{\mathrm{lin}}, \qquad (23)$$

where the expression of $K_{\mathrm{P,L}}$ and f_{lin} can be found in Neumeier [16].

A steady correction factor can also be applied (Eq. 24; see TFM - steady cutoff in Tab. 1). The correction factor beyond f_{c} is taken as $K_{\mathrm{P}}(\omega = 2\pi f_{\mathrm{c}})$ and stays the same over the whole high-frequency tail.

$$K_{\mathrm{P}}(\omega) = K_{\mathrm{P}}(\omega = 2\pi f_{\mathrm{c}}) \qquad \text{for } \frac{\omega}{2\pi} > f_{\mathrm{c}} \qquad (24)$$

In Section 4.1.1, the influence of the above high-frequency tail correction methods on wave reconstruction and parasite oscillations will be addressed. A sensitivity study over the typical *in situ* f_{c} range will be also conducted.

2.2. Semi-empirical transfer function method

To avoid introducing a cutoff frequency, several authors have proposed local methods, as opposed to global (spectral) methods, in order to improve the shape and height of individual waves. Nielsen (1986) [17] was the first to develop such methods called local sinusoidal approximation (LSA) methods.

A local frequency based on the local curvature is defined as:

$$\omega_i^2 = -\frac{(\partial_{tt}\zeta_{\mathrm{H}}^{\delta_{\mathrm{m}}})_i}{(\zeta_{\mathrm{H}}^{\delta_{\mathrm{m}}})_i} = -\frac{(\zeta_{\mathrm{H}}^{\delta_{\mathrm{m}}})_{i+1} - 2(\zeta_{\mathrm{H}}^{\delta_{\mathrm{m}}})_i + (\zeta_{\mathrm{H}}^{\delta_{\mathrm{m}}})_{i-1}}{(\zeta_{\mathrm{H}}^{\delta_{\mathrm{m}}})_i \Delta t^2} \qquad (25)$$

12

where $(\zeta_{\mathrm{H}}^{\delta_{\mathrm{m}}})_i$ is the ith value of time series $\zeta_{\mathrm{H}}^{\delta_{\mathrm{m}}}$ (Eq. 3) and $\Delta t = \dfrac{1}{f_a}$, f_a being

210   the sampling rate.

Along with a stretched linear theory, Nielsen (1986) [17] established the following semi-empirical transfer function method (see semi-empirical TFM in Tab. 1):

$$\zeta_{\mathrm{N}} = \zeta_{\mathrm{H}}^{\delta_{\mathrm{m}}} F\left[\frac{\omega^2}{g}(h_0 + \zeta_{\mathrm{H}}^{\delta_{\mathrm{m}}} - \delta_{\mathrm{m}})\right] \tag{26}$$

where the transfer function F is fitted as $F(x) = \exp\left(A\left(\dfrac{\delta_{\mathrm{m}}}{h_0}\right)x\right)$ and the empirical factor A is given by $A\left(\dfrac{\delta_{\mathrm{m}}}{h_0}\right) = 0.64 + \dfrac{0.34\delta_{\mathrm{m}}}{h_0}$.

215   Fenton (1987) [18] introduced local polynomial approximation (LPA) methods in which the complex velocity potential and the surface elevation are given by polynomials and incorporated into the fully nonlinear equations of motion. Townsend and Fenton (1997) [19] compared both LSA and LPA and concluded that LSA (Eq. 26) performs better than LPA especially for low δ_{m}/h_0 ratio.

220   Moreover, LSA requires less computational effort than LPA (Nielsen, 1989 [20]; Townsend and Fenton, 1997 [19]). Therefore, only the LSA method from Nielsen (1989) [20] is considered in this study.

13

Surface elevation name	Reconstruction method	Associated equations	Nonlinear cutoff frequency f_c	High-frequency tail correction
$\zeta_H^{\delta_m}$	Hydrostatic (equivalent to pressure measurements)	Eq. 3	No	-
$\zeta_{L,\text{space}}$	Linear formula in space	Eq. 13, 14	No	-
$\zeta_{L,\text{NC}}$	TFM	Eq. 15, 16 and 17	No	-
$\zeta_{L,\text{Sh}}$	TFM - sharp cutoff	Eq. 15, 17	Yes	Eq. 19, 20
$\zeta_{L,J}$	TFM - Jonswap	Eq. 15, 17	Yes	Eq. 19, 21
$\zeta_{L,L}$	TFM - linear cutoff	Eq. 15, 17	Yes	Eq. 19, 22, 23
$\zeta_{L,\text{St}}$	TFM - steady cutoff	Eq. 15, 17	Yes	Eq. 19, 24
ζ_N	semi-empirical TFM	Eq. 26	No	-

Table 1: Overview of the hydrostatic, TFM and semi-empirical TFM reconstruction methods studied in this article. - means that no high-frequency tail correction is applied.

2.3. Nonlinear methods

Over the past few years, several authors have gone to great lengths studying

225   nonlinear surface wave reconstruction from pressure measurements (e.g. Deconick et al., 2012 [21]; Oliveras et al., 2012 [22]; Constantin, 2012 [23]; Clamond and Constantin, 2013 [24]). Nevertheless, all these methods were derived assuming steady water waves propagating at a constant celerity and are therefore not suitable for real coastal applications.

230   However, Oliveras et al. (2012) [22] derived a heuristic reconstruction method ζ_{HE} as a function of ζ_L (here, ζ_L is the surface elevation reconstructed from the linear formula in space or from the TFM) that can be applied for irregular waves travelling at different wave celerities. For $\delta_m = 0$ (see Vasan and Oliveras, 2017 [25] if $\delta_m > 0$), ζ_{HE} is written as follows :

$$\zeta_{HE} = \frac{\zeta_L}{1 - \mathcal{F}_T^{-1}\{k\sinh(kh_0)\mathcal{F}_T\{\zeta_H^{\delta_m}\}\}}, \tag{27}$$

235   where k is computed with the dispersion relation (Eq. 17).

14

As remarked in Bonneton and Lannes (2017) [4], at order $O(\sigma)$, this formula is equivalent to :

$$\zeta_{\mathrm{HE}} = \zeta_{\mathrm{L}} - \frac{1}{g}\zeta_{\mathrm{L}}\partial_{tt}\zeta_{\mathrm{L}}. \tag{28}$$

Using data from laboratory experiments, the heuristic method was found to significantly improve the wave crest elevation as well as the wave shape compared 240 to the TFM (Oliveras et al., 2012 [22]).

Recently, Bonneton and Lannes (2017) [4] and Bonneton et al. (2018) [26] have derived nonlinear reconstruction methods also suitable for irregular waves. Bonneton and Lannes (2017) [4] performed an asymptotic expansion of the nonlinear wave equations in terms of the steepness parameter σ. For $\delta_{\mathrm{m}} = 0$ 245 (see Bonneton and Lannes, 2017 [4] if $\delta_{\mathrm{m}} > 0$) and neglecting the $O(\sigma^2)$ terms, they obtained a fully-dispersive nonlinear reconstruction method :

$$\zeta_{\mathrm{NL}} = \zeta_{\mathrm{L}} - \frac{1}{g}\partial_t(\zeta_{\mathrm{L}}\partial_t\zeta_{\mathrm{L}}). \tag{29}$$

The nonlinear term on the right-hand side of Eq. 29 can be splitted into two nonlinear terms: (1) $-\frac{1}{g}(\zeta_{\mathrm{L}}\partial_{tt}\zeta_{\mathrm{L}})$ and (2) $-\frac{1}{g}(\partial_t\zeta_{\mathrm{L}})^2$. Term (1) improves the wave extrema compared to the linear reconstruction ζ_{L} by increasing the crest 250 elevation and flattening the wave trough. Term (2), which is neglected in the heuristic method (see Eq. 28), amplifies the wave skewness and asymmetry. Both nonlinear methods described above rely on ζ_{L}. The latter can theoretically be computed using the linear formula in space $\zeta_{\mathrm{L,space}}$. Fig. 4 shows the surface elevation reconstructed from the two nonlinear methods using the linear formula 255 in space ($\zeta_{\mathrm{HE,space}}$ and $\zeta_{\mathrm{NL,space}}$, respectively; see Tab. 2).
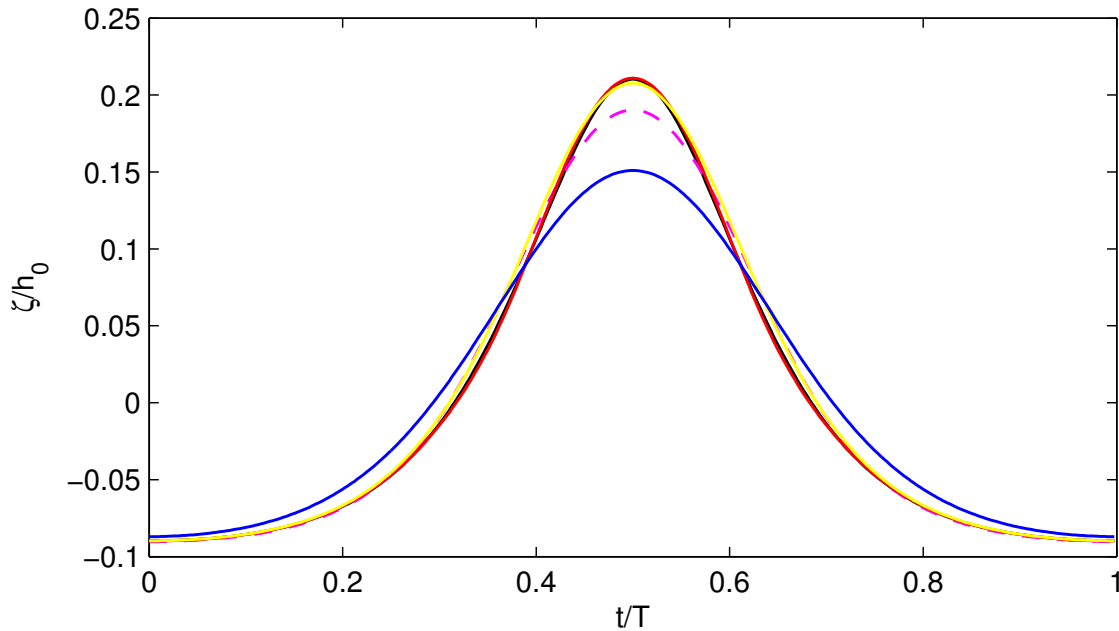
15

Figure 4: Surface elevation of a periodic weakly nonlinear wave, $\epsilon = 0.15$, $\mu = 0.25$, $\delta_{\mathrm{m}} = 0$. Full Euler solution (black line); hydrostatic reconstruction: $\zeta_{\mathrm{H}}^{\delta_{\mathrm{m}}}$ (blue line); linear formula in space: $\zeta_{\mathrm{L,space}}$ (magenta dashed line); fully-dispersive nonlinear reconstruction in space: $\zeta_{\mathrm{NL,space}}$ (red line); heuristic reconstruction in space: $\zeta_{\mathrm{HE,space}}$ (yellow line); see the associated equations in Tab. 1 and 2.

Both nonlinear methods accurately reproduce the crest elevation and the wave shape. Nonetheless, $\zeta_{\mathrm{NL,space}}$ provides a better description of the peaked wave shape as well as the crest elevation compared to $\zeta_{\mathrm{HE,space}}$. As explained in the previous section, the measured pressure P_m is often available at one single measurement point which implies to use the classical TFM instead of the linear formula in space. Hence, in practice, a cutoff frequency needs to be introduced for computing ζ_{HE} and ζ_{NL}. Bonneton and Lannes (2017) [4] have applied these nonlinear reconstructions in case of fully-dispersive nonlinear bichromatic waves ($\mu = 0.53$). Even though the heuristic method is able to properly reproduce the crest elevation, it still underestimates the skewed shape of the largest waves. The fully-dispersive nonlinear method was found to provide a much better de-

16

scription of the peaked and skewed waves than both the TFM and the heuristic reconstructions.

To overcome the need for a cutoff, in weakly-dispersive regime ($\mu << 1$), Bon-
270 neton et al. (2018) [26] made a Taylor expansion of the nonlinear wave equations with respect to μ. Neglecting the $O(\mu^2)$ terms, they obtained the following weakly-dispersive linear and nonlinear reconstruction methods (see Bonneton et al., 2018 [26] if $\delta_{\mathrm{m}} > 0$):

$$\zeta_{\mathrm{SL}} = \zeta_{\mathrm{H}}^{\delta_{\mathrm{m}}} - \frac{h_0}{2g}\partial_{tt}\zeta_{\mathrm{H}}^{\delta_{\mathrm{m}}} \tag{30}$$

$$\zeta_{\mathrm{SNL}} = \zeta_{\mathrm{SL}} - \frac{1}{g}\partial_t\left(\zeta_{\mathrm{SL}}\partial_t\zeta_{\mathrm{SL}}\right). \tag{31}$$

Along with the semi-empirical TFM (see Tab. 1), Eq. 30 and 31 can be applied
275 locally in time and a cutoff frequency is not necessarily needed, unlike for the computation of fully-dispersive methods (TFM, ζ_{HE} and ζ_{NL}). Bonneton et al. (2018) [26] applied Eq. 31 locally in time by discretizing first- and second-order time derivatives involved in Eq. 30 and 31. Such time discretization requires to filter measurement noise, as with the Fourier approach. However,
280 time derivatives computation is more accurate using Fourier analysis.

In this way, recovering ζ_{SL} and ζ_{SNL} (and ζ_{N}) still requires a cutoff frequency $f_{\mathrm{c,noise}}$ in order to remove pressure measurement noise. However, this cutoff frequency is much higher than the nonlinear cutoff frequency f_{c} introduced earlier. Accordingly, ζ_{SL} and ζ_{SNL} (and ζ_{N}) are computed accounting for much higher
285 frequency spectral information which is crucial to correctly reconstruct the surface elevation of nonlinear waves. Bonneton et al. (2018) [26] found a good agreement for weakly-dispersive nonlinear waves ($\mu < 0.3$) between ζ_{SNL} and direct ζ measurements in case of monochromatic waves ($\epsilon = 0.65$), bichromatic waves ($\epsilon = 0.37$) and *in situ* waves ($\epsilon_{max} = 0.31$ where ϵ_{max} is the nonlinear
290 parameter of the highest wave).

Surface elevation name	Reconstruction method	Associated equations	Nonlinear cutoff frequency f_c
$\zeta_{HE,space}$	Heuristic in space	Eq. 27 (using $\zeta_{L,space}$)	No
$\zeta_{NL,space}$	Fully-dispersive nonlinear in space	Eq. 29 (using $\zeta_{L,space}$)	No
ζ_{HE}	Heuristic in time	Eq. 27	Yes
ζ_{NL}	Fully-dispersive nonlinear in time	Eq. 29	Yes
ζ_{SNL}	Weakly-dispersive nonlinear	Eq. 30, 31	No

Table 2: Overview of the nonlinear reconstruction methods studied in this article.

3. *In situ* dataset

3.1. Field site

In order to assess and compare the ability of the reconstruction methods to recover irregular wave field from pressure measurements, *in situ* hydrodynamic

295   data was collected at La Salie beach, SW France (see Fig. 5). La Salie beach is a relatively alongshore-uniform gently-sloping sandy beach associated with a meso-macro semi diurnal tidal regime. The relatively wide intertidal region ($\sim$ 200 m in the cross-shore) allows easy and convenient instrument deployment at low tide.

Figure 5: (a) Location map with the field site of La Salie indicated by the black circle. (b) Unmanned aerial vehicle photo of the field site at mid-tide during the experiment. A video system was installed on the pier shown in the left-hand side of the image. The yellow star and the red star show the location of the video system and the instrument, respectively, during the experiment.

3.2. Field experiment

The field experiment was carried out over two periods on April 13-14 2017 (LS1) and May 17-18 2018 (LS2) and aimed at characterizing nonlinear waves in intermediate and shallow depth. A Nortek Signature 1000 kHz current profiler was deployed at low tide. The Signature 1000 kHz vertical beam allows a high-frequency direct measurement of the surface wave elevation using Acoustic Surface Tracking (AST). Besides AST, it also provides pressure measurements. Signature 1000 manufacturer (Nortek) reports pressure-derived elevation and AST measurements with accuracy of $\pm$ 1 mm and $\pm$ 2 cm, respectively. The instrument recorded at 8 Hz sampling rate and pressure was measured at 0.7 m above the bottom ($\delta_{\mathrm{m}} = 0.7$ m). The characteristic bottom slope was $\sigma_b = 0.015$ at the sensor location.

AST is a relatively new ADCP feature that has mainly been validated for waves propagating in deep water (> 20 m) and for sampling rate not exceeding 4 Hz

19

(Pedersen and Nylund, 2004 [27]; Pedersen and Lohrmann, 2004 [28]). Martins

315 et al. (2017) [29] collected high-frequency surface elevation measurements and found a very good agreement between the surface elevation measured from the Signature 1000 kHz and from a LIDAR scanner (root mean square error RMSE of 0.05 m) for an undular tidal bore propagating in the Garonne river ($\epsilon = 0.08$; $\mu = 5.85$; the mean water depth at low tide was 2.8 m).

320 Nonetheless, AST is very sensitive to air bubbles as the acoustic signal can be significantly altered within the water column (see Nortek Manual [30]). Hence, the AST ability to provide reliable measurements under wave breaking can be questioned (Pedersen et al., 2002 [31]; Birch et al., 2004 [32]), but the present study focuses on waves propagating outside the surf zone (see Fig. 6). A video

325 system was set up on the first day of each deployment period to follow the position of the surf zone during the experiment. The system allowed to identify the time evolution of the outer edge of the surf zone, defined as the location of the onset of breaking of the largest waves (see darker points in Fig. 6, within which none of the waves are breaking). The other outer surf zone limits were

330 set by visually checking the AST signal.

Both pressure and AST measurements were divided into 10-minute time series. Pressure time series was low-pass filtered (1 Hz) to remove instrumental noise. AST time series was also low-pass filtered to be consistent with pressure time series. The mean water depth h_0 was computed from pressure measurements both

335 outside and inside the surf zone. Each water depth time series was detrended to remove tidal variation. The water level was slowly fluctuating with the infragravity motion. We then define the free surface elevation (in the short-wave frequency band) as :

$$\zeta(t) = h(t) - h_{\mathrm{infra}}(t), \tag{32}$$

where h is the water depth and h_{infra} is the water depth computed over the

340 infragravity frequency range (0.005 Hz - 0.05 Hz). Eq. 32 was applied to both pressure and AST measurements yielding the hydrostatic surface elevation $\zeta_{\mathrm{H}}^{\delta_{\mathrm{m}}}$

20

(Eq. 3) and the direct measurement of the surface elevation ζ_m, respectively. Outside the surf zone, h_0 ranged from 2.25 m to 3.72 m (see Fig. 6a). For such water depths, we choose to take $n = 4$ (as in Jones and Monismith, 2007 [13]) for

345 the TFM - Jonswap method (Eq. 21). Except for h_0, parameters in Fig. 6 were calculated using $\zeta_\mathrm{H}^{\delta_\mathrm{m}}$ inside the surf zone and using ζ_m outside the surf zone. Both experiments were characterized by long and grouped wave conditions with a sea-swell significant wave height $H_\mathrm{s,short\text{-}wave}$ ranging from 0.54 m to 1.08 m (see Fig. 6b) associated with a peak period T_P ranging from 8.6 s to 11.5 s (see

350 Fig. 6c). The maximum observed wave height was 1.54 m for LS1 and 1.95 m for LS2. The wave number k was estimated using the linear dispersion relation (Eq. 17) yielding the shallowness parameter $\mu = (kh_0)^2$. The whole dataset features relatively small μ ($\mu \leq 0.2$; see Fig. 6d) characterizing a weakly-dispersive wave regime. It is worth noting that, the parameter $\sqrt{\mu}\sigma_b$ being very small for the

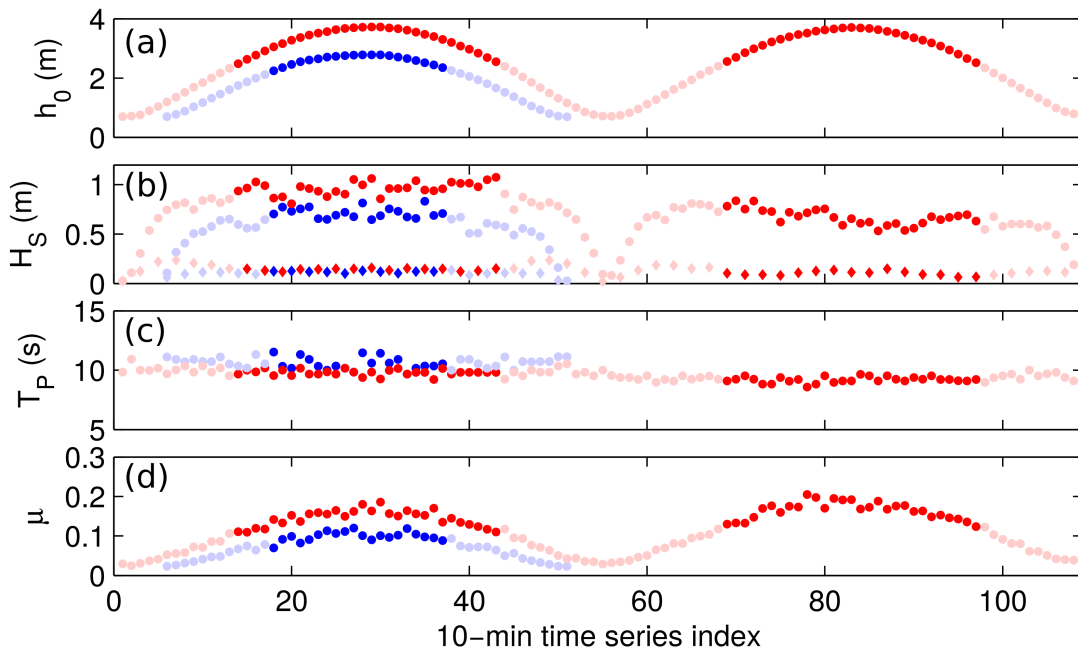355 whole experiment, the bottom contribution can be neglected (Bonneton et al., 2018 [26]).

21

Figure 6: Wave and tide conditions for both experiments (LS1 in blue and LS2 in red). (a) Mean water depth h_0; (b) Short-wave significant wave height $H_{s,\text{short-wave}}$ (circles) and infragravity significant wave height $H_{s,\text{infra}}$ computed over 20 min (diamonds); (c) Spectral peak period T_P; (d) Shallowness parameter μ. Dark-colored points and light-colored points show data outside and inside the surf zone, respectively. Transitions between both areas represent the outer surf zone limits. In the present study, we only focus on the dark-colored points.

3.3. Data processing

3.3.1. AST processing

Even outside the surf zone, the AST signal was sometimes altered by reflection within the water column. This was caused by the presence of air bubbles that were generated by wave breaking occurring shoreward but close to the instrument, which were occasionally moved by currents above the instrument. This led to the presence of spikes in the surface wave elevation time series that were removed using a gradient thresholds between two consecutive points.

22

₃₆₅ *3.3.2. Wave-by-wave analysis*

Zero crossing analysis is the most traditional method to determine individual wave characteristics. It first consists in identifying individual waves between each zero-downcrossing or each zero-upcrossing of surface wave elevation. Wave crests and troughs are then respectively defined as the maximum and minimum ₃₇₀ of surface elevation between two consecutive crossings. In intermediate depth to shallow water, low-frequency motions can be strong and might potentially lead to crests under the mean sea level and troughs above the mean sea level, making the zero-crossing method irrelevant. In addition, filtering-out low-frequency motions is not a reliable option as it can critically transform the wave extrema ₃₇₅ and the wave shape (Power et al., 2010 [33]). A different method based on a local maxima analysis was implemented (Power et al. 2010 [33]; Power et al. 2015 [34]; Martins et al., 2017 [5]). A wave is identified between two consecutive crests. The wave trough is taken as the minimum of the surface elevation between the two consecutive crests. Wave height and period criteria are set to ₃₈₀ avoid detecting small oscillations (with amplitude < 0.1 m and period $< T_P/4$).

4. Results and discussion

In this section, the different reconstruction methods presented above are applied to LS1 and LS2 dataset and further compared (see Tab. 1 and 2). We first assess each method in near-breaking conditions. These conditions are characterized by ₃₈₅ the presence of nonlinear waves for which the validity of linear reconstruction methods to recover individual wave characteristics is questionable. Then, the ability of each method to recover waves within wave groups which contain highly nonlinear and extreme waves is addressed. Finally, we present a wave-by-wave analysis over the whole dataset.

₃₉₀ *4.1. Near-breaking conditions*

In this subsection, we focus on a 10-minute time series from LS1 characterized by highly nonlinear waves, i.e. waves just before the onset of breaking (see the

blue point at the first outer surf zone limit of LS1 in Fig. 6; $h_0 = 2.25$ m; μ
= 0.075). This time series is characterized by a peak wave period of 11.5 s, a
395   significant wave height of 0.71 m and a maximum individual wave height of 1.4
m. The latter yields a maximum nonlinearity parameter ϵ of 0.31 corresponding
to strong *in-situ* nonlinearities.

4.1.1. Linear methods and semi-empirical transfer function

Surface elevation energy density spectra computed from the TFM with differ-
400   ent high-frequency tail corrections and the semi-empirical TFM (see Tab. 1)
are presented in Fig. 7. Here, the nonlinear cutoff frequency f_c is set at 0.32
Hz which corresponds to frequency up to the third harmonic (around 0.28 Hz).
As explained in Section 2, the cutoff frequency associated with spectral recon-
struction methods is optimized. Indeed, it is set by comparing the wave energy
405   reconstructed from the TFM - no cutoff ($\zeta_{L,NC}$) and the true wave energy (ζ_m).
f_c is taken at the frequency for which the TFM correction starts exceeding the
measured wave energy. Again, results are very sensitive to f_c. Depending on its
value, the computed wave surface elevation can be significantly altered, which
will be addressed at the end of this section.

410   As expected, $\zeta_H^{\delta_m}$ correctly reproduces the low-frequency spectrum as well as
the first harmonic (around 0.09 Hz) but strongly underestimates the energy
of all subsequent harmonics. The semi-empirical TFM, ζ_N, provides a good
estimate of wave energy up to the second harmonic (around 0.18 Hz) but then
slowly starts underpredicting all the subsequent harmonics as well. For $f < f_c$,
415   the TFM - sharp cutoff, $\zeta_{L,SH}$, (equivalent to $\zeta_{L,L}$, $\zeta_{L,ST}$ and $\zeta_{L,J}$) properly
reproduces the energy spectrum compared to $\zeta_H^{\delta_m}$.
For $f > f_c$, $\zeta_{L,SH}$ (equivalent to $\zeta_H^{\delta_m}$) strongly underestimates the energy by two
to three orders of magnitude at the highest frequencies. The TFM - Jonswap,
$\zeta_{L,J}$, is able to reproduce the high-frequency tail's slope but does not reconstruct
420   any harmonics. In the other hand, both the TFM - linear cutoff and the TFM -
steady cutoff, $\zeta_{L,L}$ and $\zeta_{L,ST}$ respectively, improve $\zeta_{L,SH}$ by correctly recovering
one extra harmonic (fourth harmonic around 0.36 Hz), even though the energy

24

is slightly underestimated. Unlike $\zeta_{\mathrm{L,ST}}$ that keeps correcting $\zeta_{\mathrm{L,SH}}$ over all frequencies, $\zeta_{\mathrm{L,L}}$ fades into $\zeta_{\mathrm{L,SH}}$ around 0.7 Hz.
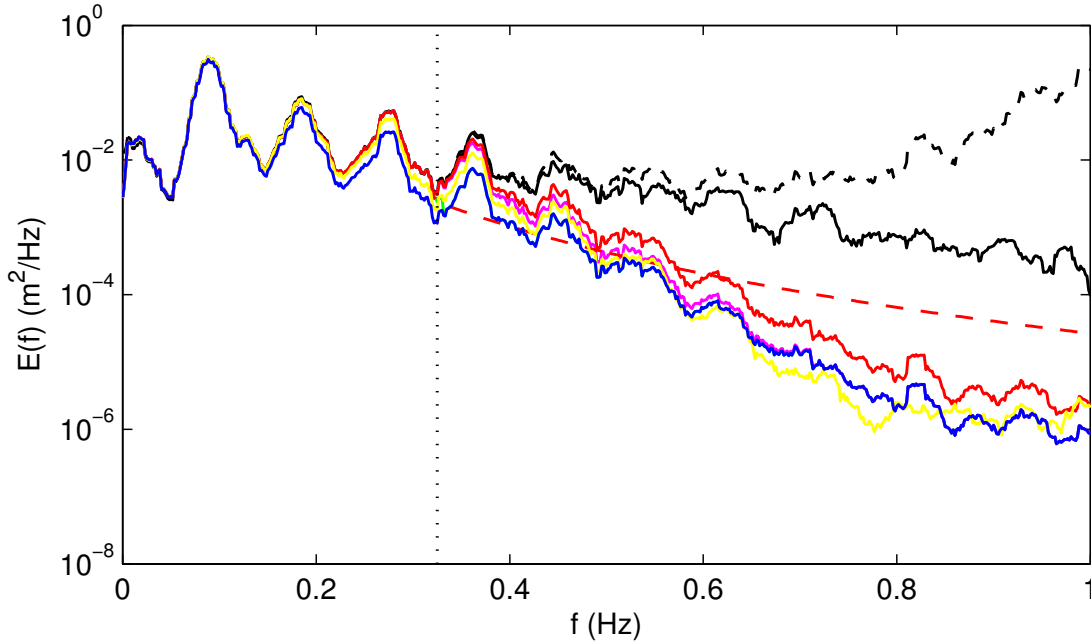

Figure 7: Surface elevation energy density spectra E(f). AST measurements: ζ_{m} (black line); hydrostatic reconstruction: $\zeta_{\mathrm{H}}^{\delta_{\mathrm{m}}}$ (blue line); TFM - sharp cutoff: $\zeta_{\mathrm{L,SH}}$ (green line); TFM -linear cutoff: $\zeta_{\mathrm{L,L}}$ (magenta line); TFM - steady cutoff: $\zeta_{\mathrm{L,ST}}$ (red line); TFM - Jonswap: $\zeta_{\mathrm{L,J}}$ (red dashed line); TFM - no cutoff $\zeta_{\mathrm{L,NC}}$ (black dashed line); semi-empirical TFM: ζ_N (yellow line); see the associated equations in Tab. 1 $f_{\mathrm{c}} = 0.32$ Hz (vertical black dotted line). The spectra have been averaged over 1/66 Hz.

425   The relative error of the spectral significant wave height $H_{\mathrm{m0}} = 4\sqrt{m_0}$ (where m_0 is the zero-th spectral moment calculated between 0 and 1 Hz), the maximal crest elevation $(\zeta_{\mathrm{c}})_{\mathrm{max}}$ and the skewness parameter $S_{\mathrm{k}} = <\zeta^3>/(<\zeta^2>)^{3/2}$ (where $<.>$ is the time-averaging operator) are computed for each reconstruction formula (see Tab. 3). In terms of H_{m0}, all TFM as well as the semi-empirical

430   TFM are significantly better than $\zeta_{\mathrm{H}}^{\delta_{\mathrm{m}}}$ (equivalent to pressure measurements) and lead to reasonable H_{m0} error (≤ 7.4 %) which is in line with the literature (e.g. Guza and Thornton, 1980 [2]; Bishop and Donelan, 1987 [1]). ζ_{N} provides

25

the same H_{m0} as $\zeta_{L,SH}$. Both $\zeta_{L,L}$ and $\zeta_{L,ST}$ are better than $\zeta_{L,SH}$ by roughly 2 %. As $\zeta_{L,J}$ strongly underestimates the fourth and fifth harmonics (around

435   0.36 and 0.45 Hz in Fig. 7), the computed H_{m0} error is slightly higher than all other linear reconstructions. Among all reconstructions, $\zeta_{L,ST}$ has the lowest H_{m0} error.

	$\zeta_H^{\delta_m}$	$\zeta_{L,SH}$	$\zeta_{L,L}$	$\zeta_{L,ST}$	$\zeta_{L,J}$	ζ_N
H_{m0}	14.6	7.1	5.7	5.1	7.4	7.1
$(\zeta_c)_{max}$	41.8	33.7	28.6	26.5	-	30.6
S_k	59.9	49.5	41.0	37.2	-	42.0

Table 3: Spectral significant wave height H_{m0}, highest crest elevation $(\zeta_c)_{max}$ and sea surface skewness S_k relative error (%). hydrostatic reconstruction: $\zeta_H^{\delta_m}$; TFM - sharp cutoff: $\zeta_{L,SH}$; TFM - linear cutoff: $\zeta_{L,L}$; TFM - steady cutoff: $\zeta_{L,ST}$; TFM - Jonswap: $\zeta_{L,J}$; semi-empirical TFM: ζ_N; see the associated equations in Tab. 1. $f_c = 0.32$ Hz.

The same trend is observed for temporal parameters $(\zeta_c)_{max}$ and S_k. In terms of these parameters, ζ_N performs roughly the same as $\zeta_{L,SH}$. The TFM is slightly

440   improved using the linear cutoff and the steady cutoff approaches ($\zeta_{L,L}$ and $\zeta_{L,ST}$, respectively). Nonetheless, $\zeta_{L,ST}$, which gives the best agreement with ζ_m, still considerably underestimates both $(\zeta_c)_{max}$ and S_k by 26.5 % and 37.2 %, respectively (see Tab. 3).

For the sake of clarity, we only display in Fig. 8 the water depth time series re-

445   constructed from the TFM - sharp cutoff and the TFM - steady cutoff (the latter giving the best results among all linear reconstructions). In line with the errors shown in Tab. 3, both reconstructions are able to recover the smallest waves but they strongly underestimate the peaked and skewed shape of the highest waves within the group, even though $\zeta_{L,ST}$ slightly improves the reconstructed

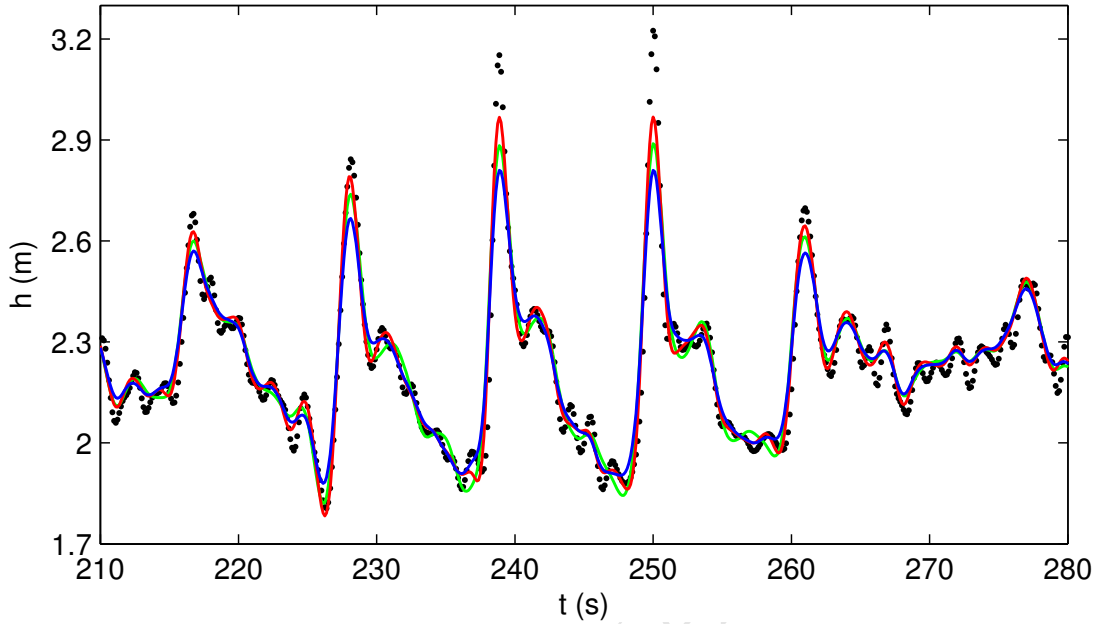450   crest elevation compared to $\zeta_{L,SH}$.

Figure 8: Water depth time series of a wave group. AST measurements: $h_0 + \zeta_m$ (black points); hydrostatic reconstruction: $h_0 + \zeta_H^{\delta_m}$ (blue line); TFM - sharp cutoff: $h_0 + \zeta_{L,SH}$ (green line); TFM - steady cutoff: $h_0 + \zeta_{L,ST}$ (red line); see the associated equations in Tab. 1. $f_c = 0.32$ Hz and $h_0 = 2.25$ m.

In most studies involving surface elevation recovery from pressure sensors, the rationale for choosing a particular f_c value is often unclear. To assess the cutoff frequency sensitivity, we set f_c at 0.6 Hz, which corresponds to the highest value found in the literature. Fig. 9 shows the effect on the wave energy spectrum. With such cutoff frequency, the section of the wave energy between 0.32 Hz and 0.6 Hz computed from $\zeta_{L,SH}$ is overestimated. This drawback is strengthened for $\zeta_{L,L}$ and $\zeta_{L,ST}$ because these methods (Eq. 22, 23 and 24) already fill the high-frequency tail. In Fig. 9, this is particularly noticeable for $\zeta_{L,ST}$ which overestimates the harmonic around 0.61 Hz. As the reconstructed energy is higher, the H_{m0} error is much lower (1.4 % for $\zeta_{L,SH}$ and 0.4 % for $\zeta_{L,ST}$).

As shown in Fig. 10, due to the energy overestimation, the crest elevation of each wave is artificially enhanced and the reconstructed time series is affected by stronger parasite oscillations compared to $f_c = 0.32$ Hz. These oscillations

27

severely transform the shape of the surface wave elevation, particularly within

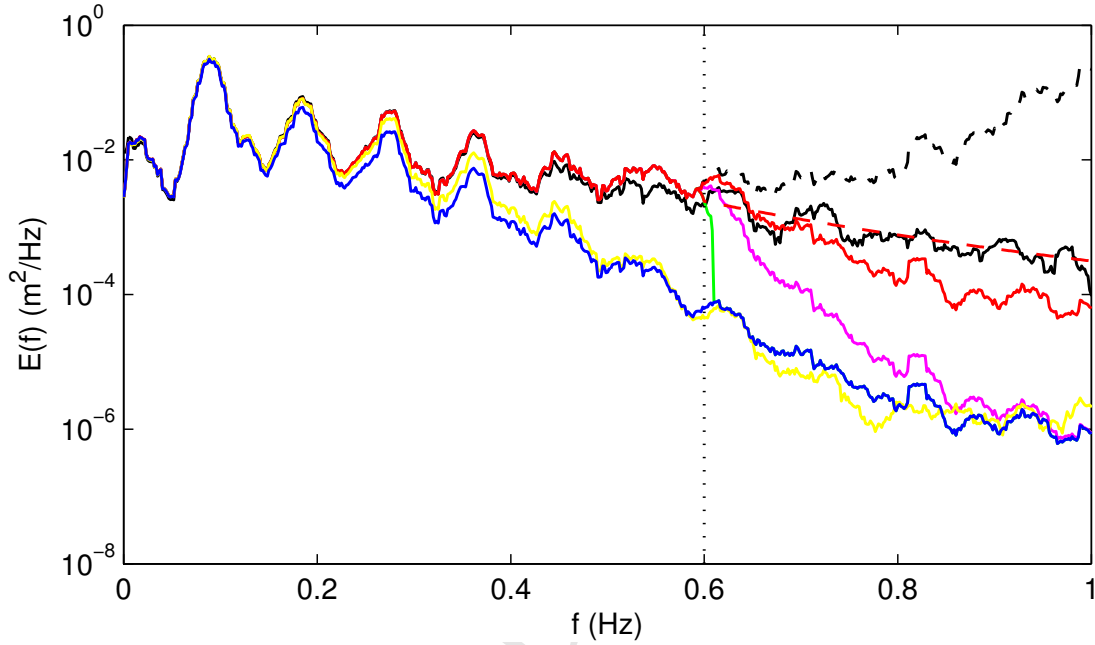465 the back face and the trough of the highest waves (see for instance at t = 236 and 252 s in Fig. 10).

Figure 9: Surface elevation energy density spectra E(f). AST measurements: ζ_m (black line); hydrostatic reconstruction: $\zeta_H^{\delta_m}$ (blue line); TFM - sharp cutoff: $\zeta_{L,SH}$ (green line); TFM - linear cutoff: $\zeta_{L,L}$ (magenta line); TFM - steady cutoff: $\zeta_{L,ST}$ (red line); TFM - Jonswap: $\zeta_{L,J}$ (red dashed line); TFM - no cutoff $\zeta_{L,NC}$ (black dashed line); semi-empirical TFM: ζ_N (yellow line); see the associated equations in Tab. 1 $f_c = 0.6$ Hz (vertical black dotted line). The spectra have been averaged over 1/66 Hz.
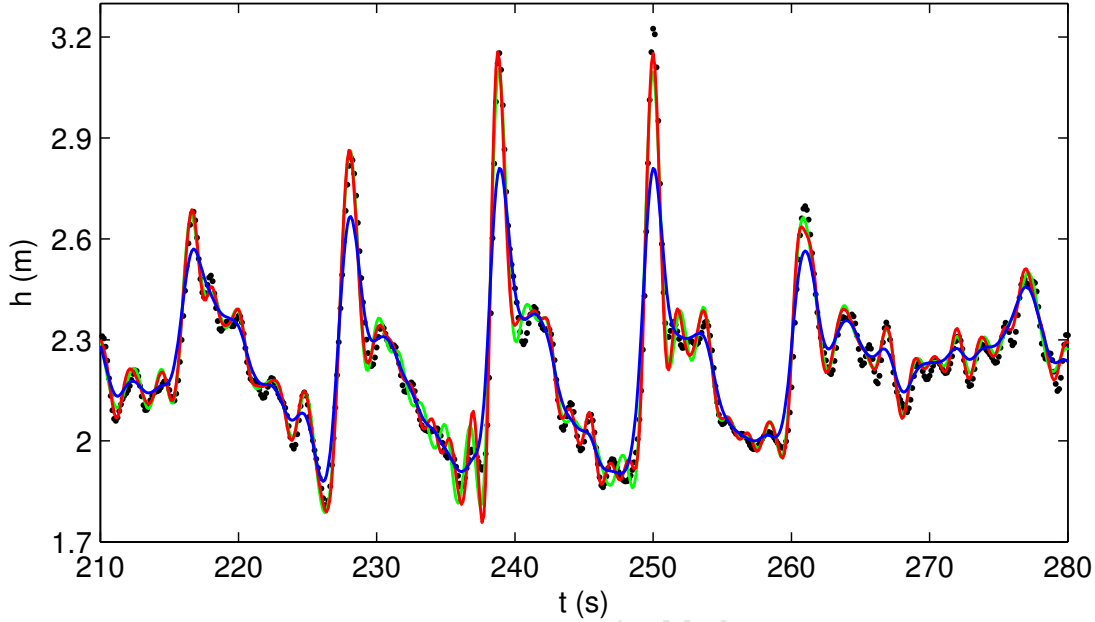
Figure 10: Water depth time series of a wave group. AST measurements: $h_0 + \zeta_m$ (black points); hydrostatic reconstruction: $h_0 + \zeta_H^{\delta_m}$ (blue line); TFM - sharp cutoff: $h_0 + \zeta_{L,SH}$ (green line); TFM - steady cutoff: $h_0 + \zeta_{L,ST}$ (red line); see the associated equations in Tab. 1. $f_c = 0.6$ Hz and $h_0 = 2.25$ m.

These results show that the classical TFM predicts the significant wave height with reasonable accuracy even when waves are nonlinear (see H_{m0} in Tab. 3). The different high-frequency tail correction methods associated with the TFM

470 (see Tab. 1) lead to lower H_{m0} error by artificially amplifying the high-frequency wave spectrum. However, in terms of individual wave characteristics, all linear reconstruction methods reviewed here show similar skill. They significantly underestimate the crest elevation of the highest waves as well as its skewed shape. In the following, only the TFM with a sharp high-frequency tail correction (see

475 TFM - sharp cutoff in Tab. 1), hereafter referred to as ζ_L, is used for systematic comparison with nonlinear methods.

29

4.1.2. Nonlinear methods

Reconstructed surface elevation energy and time series from each nonlinear method (except for ζ_{NL} for the sake of clarity) are presented in Fig. 11, 12
480 and 13. As explained in Section 3.2, pressure time series (equivalent to $\zeta_{\mathrm{H}}^{\delta_{\mathrm{m}}}$ Eq. 3) were low-pass filtered to remove instrumental noise. The cutoff frequency associated with this filter is the cutoff frequency $f_{\mathrm{c,noise}}$ set to 1 Hz here. This cutoff frequency is applied to compute the weakly-dispersive methods ζ_{SL} and ζ_{SNL}. $f_{\mathrm{c,noise}}$ is much higher than the nonlinear cutoff frequency, used for the
485 fully-dispersive methods ($f_{\mathrm{c}} = 0.32$ Hz). This makes the fully-dispersive methods much more restrictive than the weakly-dispersive methods and the high-frequency tail is better predicted by ζ_{SL} and ζ_{SNL} than by ζ_{L} and ζ_{HE} (see Fig. 11). As both the heuristic method and the fully-dispersive nonlinear method rely on the TFM which requires a nonlinear cutoff frequency, ζ_{HE} and ζ_{NL} do
490 not improve enough ζ_{L} and lead to larger errors compared to ζ_{SNL} (see Tab. 4). Even if ζ_{SL} and ζ_{SNL} slightly underestimate the second and third harmonics, the energy distribution in the highest frequencies is well evaluated leading to an accurate calculation of H_{m0} for both methods (error of 6.3 % and 4.2 %, respectively; see Tab. 4). Taking nonlinear effects into account, the SNL method
495 accurately reproduces the energy over a large number of harmonics compared to the SL method. Beyond 0.6 Hz, ζ_{SNL} is considerably better than the classical TFM ζ_{L} (equivalent to $\zeta_{\mathrm{H}}^{\delta_{\mathrm{m}}}$ in this frequency range) by two orders of magnitude. The third harmonic computed from the heuristic method is slightly overestimated leading to a smaller H_{m0} error than the TFM (see Tab. 4) but
500 the energy distribution beyond f_{c} is poorly computed in the highest frequencies as it relies on the TFM. In terms of H_{m0}, ζ_{SNL} has the lowest error of all reconstruction methods reviewed in this article (see Tab. 4).
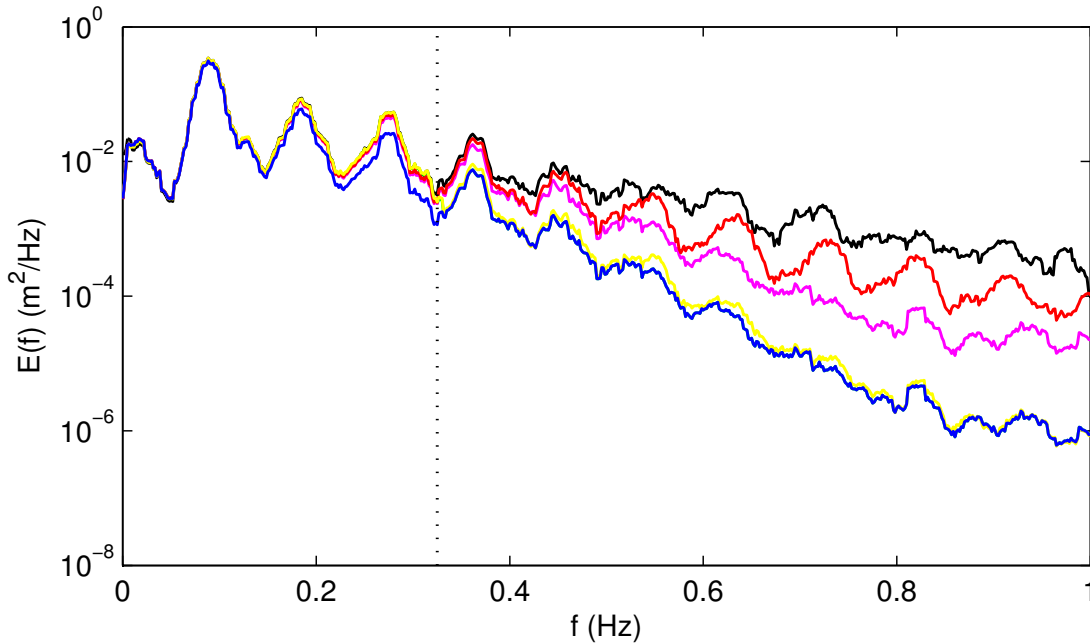
30

Figure 11: Surface elevation energy density spectra E(f). AST measurements: ζ_m (black line); hydrostatic reconstruction: $\zeta_H^{\delta_m}$ (blue line); weakly-dispersive linear reconstruction: ζ_{SL} (magenta line); weakly-dispersive nonlinear reconstruction: ζ_{SNL} (red line); heuristic reconstruction: ζ_{HE} (yellow line); see the associated equations in Tab. 2. $f_c = 0.32$ Hz (vertical black dotted line) and $f_{c,noise} = 1$ Hz. The spectra have been averaged over $1/66$ Hz.

The ability of the weakly-dispersive methods to calculate the energy distribution is reflected in the surface elevation time series (see Fig. 12 and 13). Compared to
505 ζ_L and ζ_{HE}, the weakly-dispersive reconstructions do not result in any parasite oscillation (see Fig. 12). ζ_{SNL} reproduces very well the wave crests even for the highest wave with an error of 7.1 % (see Tab. 4). The wave shape is also properly recovered especially the steep slope of the front and back face of the highest wave (see the zoom of the highest wave in Fig. 13), which translates
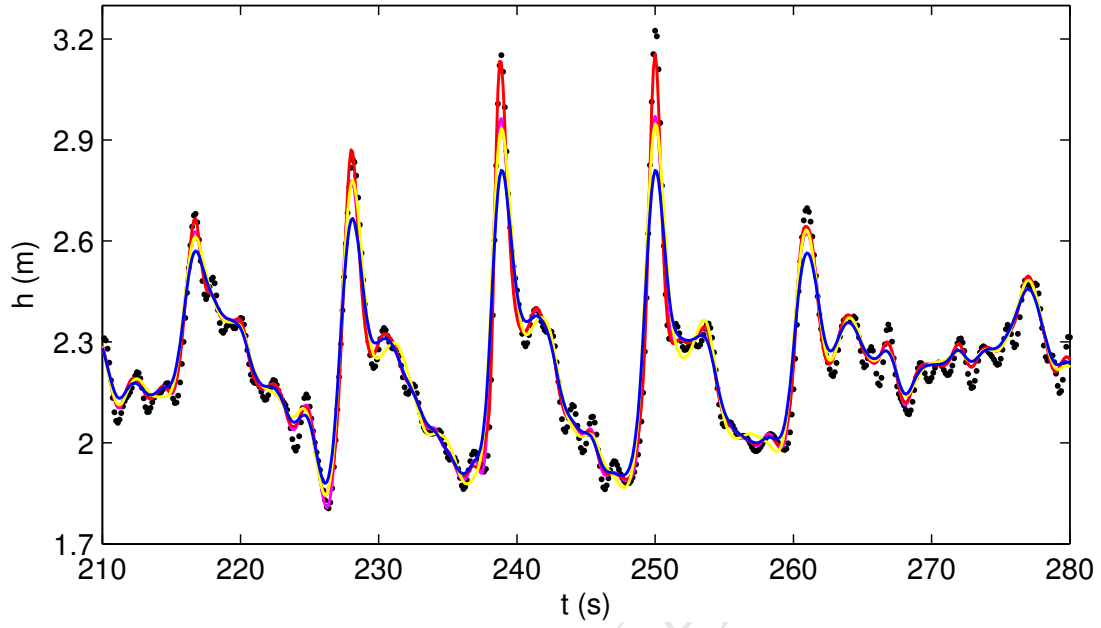510 into the lowest skewness error compared to ζ_{HE} and ζ_{SL}.

31

Figure 12: Water depth time series of a group of waves. AST measurements: ζ_m (black points); hydrostatic reconstruction: $\zeta_H^{\delta_m}$ (blue line); weakly-dispersive linear reconstruction: ζ_{SL} (magenta line); weakly-dispersive nonlinear reconstruction: ζ_{SNL} (red line); heuristic reconstruction: ζ_{HE} (yellow line); see the associated equations in Tab. 2. $f_c = 0.32$ Hz, $f_{c,noise} = 1$ Hz and $h_0 = 2.25$ m.
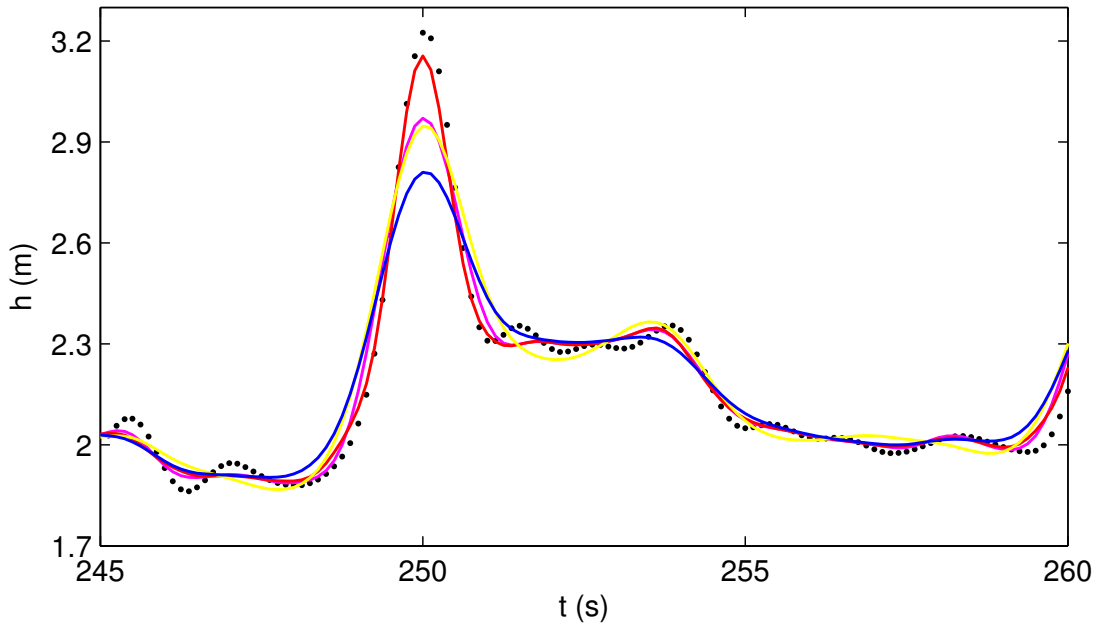
Figure 13: Water depth time series of the highest wave. AST measurements: ζ_m (black points); hydrostatic reconstruction: $\zeta_\mathrm{H}^{\delta_\mathrm{m}}$ (blue line); weakly-dispersive linear reconstruction: ζ_SL (magenta line); weakly-dispersive nonlinear reconstruction: ζ_SNL (red line); heuristic reconstruction: ζ_HE (yellow line); see the associated equations in Tab. 2. $f_\mathrm{c} = 0.32$ Hz, $f_\mathrm{c,noise} = 1$ Hz and $h_0 = 2.25$ m.

	ζ_L	ζ_HE	ζ_NL	ζ_SL	ζ_SNL
H_m0	7.1	5.7	5.9	6.3	4.2
$(\zeta_\mathrm{c})_\mathrm{max}$	33.7	28.6	26.5	25.5	7.1
S_k	49.5	34.8	29.9	37.8	7.5

Table 4: Spectral significant wave height H_m0, highest crest elevation $(\zeta_\mathrm{c})_\mathrm{max}$ and sea surface skewness S_k relative error (%). TFM - sharp cutoff ζ_L; heuristic reconstruction ζ_HE; fully-dispersive nonlinear reconstruction ζ_NL; weakly-dispersive linear reconstruction ζ_SL; weakly-dispersive nonlinear reconstruction ζ_SNL; see the associated equations in Tab. 1 and 2.

Among all reconstruction methods presented in this work, ζ_SNL is found to provide the best agreement with the measured surface elevation ζ_m regarding spectral wave parameters (H_m0) and more importantly regarding individual

33

wave characteristics ($(\zeta_c)_{max}$ and S_k). In the wave groupiness section below,

515 only the commonly-used transfer function method ζ_L (TFM - sharp cutoff) and the weakly-dispersive nonlinear method ζ_{SNL} are used.

4.1.3. Wave groupiness

Earlier studies have proven that the presence of wave groups and the infragravity wave generation are both related (Longuet-Higgins and Stewart, 1962 [35];

520 Symonds et al., 1982 [36]). It is also well known that infragravity waves can result in coastal erosion and inondation events during extreme wave conditions (Roelvink et al., 2009 [37]; Baumann et al., 2017 [38]; Bertin et al., 2018 [39]). Well predicting wave groupiness is then of paramount importance for coastal applications. Along with the measured infragravity waves, Fig. 14a shows the

525 measured wave envelope computed as the low-pass-filtered Hilbert transform of the short-wave signal (Battjes et al., 2009 [40]), with the corresponding time series of reconstructed dimensionless crest and trough elevation shown in Fig. 14b. The dimensionless crest elevation,

$$\epsilon_i = \frac{\zeta_c}{h_0} \tag{33}$$

can be considered as a local nonlinearity parameter (where ζ_c is the crest eleva-

530 tion of each individual wave). Fig. 14b shows the time series of both measured and reconstructed ϵ_i ($(\epsilon_i)_m$, $(\epsilon_i)_L$ and $(\epsilon_i)_{SNL}$, respectively). $(\epsilon_i)_m$ has an average value of 0.16 but peaks at much higher values (between 0.35 and 0.51) within the three wave groups (see at $t = 250$ s, 400 s and 760 s in Fig. 14b). Waves within these groups are highly nonlinear and also meet the following criteria:

$$\frac{\zeta_c}{H_s} > 1.25 \tag{34}$$

535 where H_S is the significant wave height, here defined as four times the standard deviation of the surface elevation. Criteria 34 is commonly used for identifying extreme waves (Dysthe et al., 2008 [41]). These highly nonlinear extreme waves also correspond to waves where the SNL correction is the most skillful compared

34

to the linear (TFM) correction in terms of dimensionless crest elevations. The
average of the highest one-tenth dimensionless crest elevations $(\epsilon_i)_{1/10}$ is under-
estimated by 30.0 % and by 2.5 % for the linear and SNL method, respectively.
By visually checking images recorded from the video system, the most nonlinear
wave over this 10-min time series $(((\epsilon_i)_m)_{max} = 0.51)$ is just before the onset of
breaking. Over the whole dataset, the highest value of $(\epsilon_i)_m$ is 0.53 outside of
the surf zone, corresponding to a wave that is even closer to breaking. Hence,
well predicting these waves is crucial for estimating the break point position
which is a key parameter to many coastal applications and wave propagation
models. At the individual wave scale, its prediction can significantly differ using
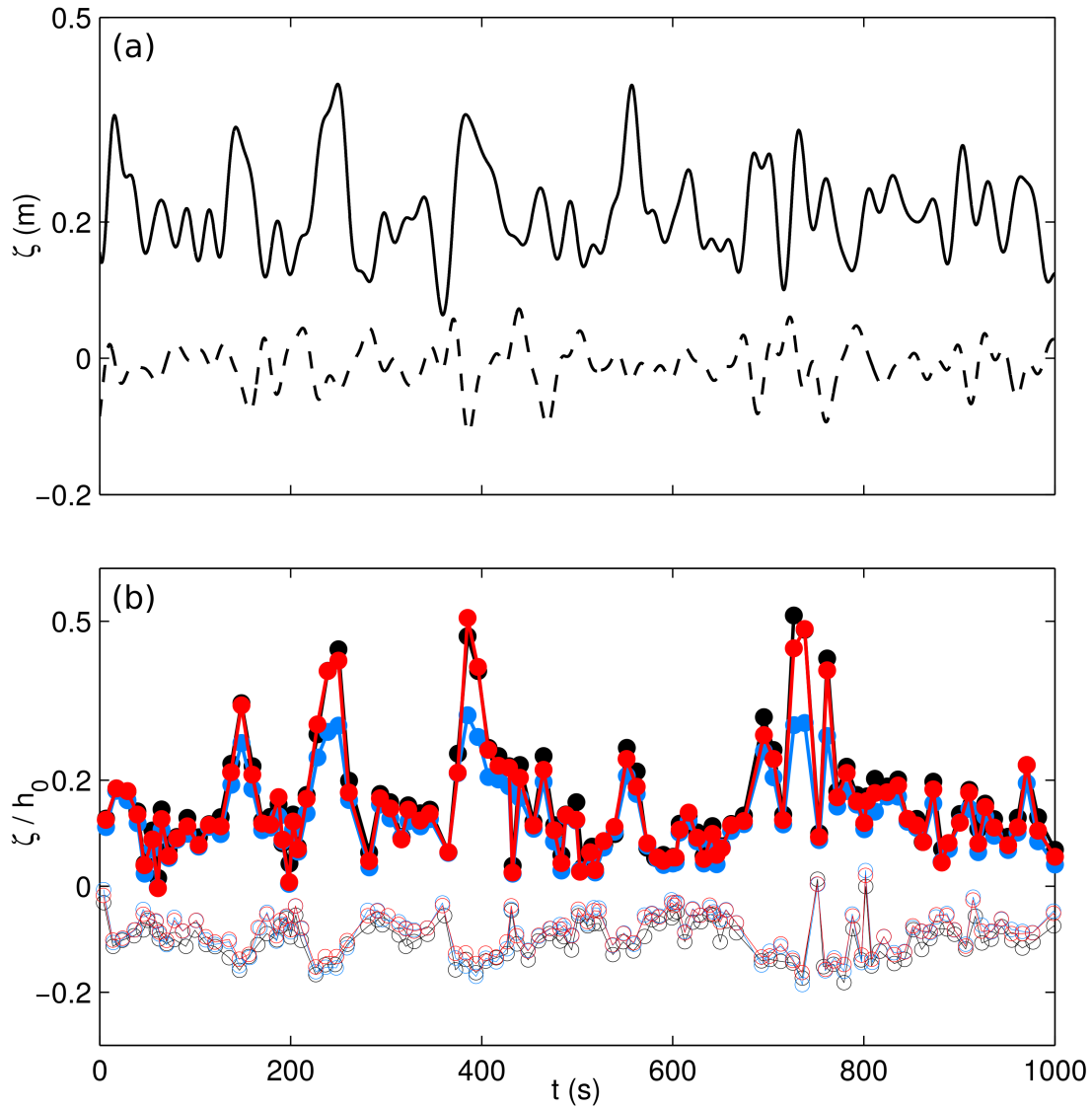the linear or the SNL reconstruction method (see wave groups in Fig. 14b).

35

Figure 14: (a) Measured wave envelope (black line) and measured infragravity surface elevation (black dashed line). (b) Dimensionless wave crests (filled circles) and troughs (empty circles) elevation. AST measurements: ζ_m (black circles); TFM - sharp cutoff ζ_L (blue circles); weakly-dispersive nonlinear reconstruction ζ_{SNL} (red circles); see the associated equations in Tab. 1 and 2. $f_c = 0.32$ Hz, $f_{c,\text{noise}} = 1$ Hz and $h_0 = 2.30$ m.

550   As pointed out above, the linear and weakly-dispersive nonlinear methods show

36

similar skill to retrieve the significant wave height (see H_{m0} error in Tab. 3 and 4). However, at the scale of individual waves, the two methods show strongly different reconstruction, especially for highly nonlinear waves in the groups, within which some waves can be characterized as extreme (see criteria 34). Ac-

555 cordingly, in the following section, a wave-by-wave analysis of the whole dataset is conducted in order to identify these nonlinear extreme waves and to further conclude on the overall ability of each method.

4.2. A wave-by-wave analysis of the whole dataset

In this section, a wave-by-wave analysis of the entire dataset is performed. For 560 each time series, relative errors for both linear and SNL reconstruction methods are computed in terms of three parameters: the root-mean-square crest elevation $(\zeta_c)_{RMS}$, the average of the highest one-tenth crest elevation $(\zeta_c)_{1/10}$ and the skewness parameter S_k. Those are represented in Fig.15 as a function of the average nonlinear parameter ϵ_m computed as :

$$\epsilon_m = \frac{(H_m)_{RMS}/2}{h_0} \qquad (35)$$

565 where $(H_m)_{RMS}$ is the measured root-mean-square wave height. AST measurements allow to detect the wave crest of all individual waves of the entire dataset. Of note, in a limited number of 10-minute time series some surface elevation was missing locally in the front faces. For these time series, S_k could not be calculated properly.

570 For the linear reconstruction, the relative error $(\zeta_c)_{RMS}$ increases with increasing ϵ_m. For low ϵ_m (< 0.10), the RMS crest elevation error (see Fig. 15a) is less than 10 %. The results of SNL method are roughly equivalent to those of the linear reconstruction, even though the SNL method gives slightly smaller errors for low ϵ_m. As nonlinearities increase, the difference between both methods 575 becomes stronger with SNL error varying around 5 to 10 % while TFM error hovers around 15 to 25 % for the highest ϵ_m (> 0.14).

This pattern is strengthened for $(\zeta_c)_{1/10}$ (see Fig. 15b). For low ϵ_m, the SNL method is better than the linear method by 3 to 5 %. Both methods quickly

37

deviate for moderate to strong nonlinearities. For the highest ϵ_m, the SNL
method is significantly better than the linear method by 13 to 28 %.

In terms of S_k (see Fig.15c), the linear reconstruction fails to correctly describe
the skewed wave shape with a scattered S_k error between 16.6 % and 51.7 %
and an average error of 29.4 %. Indeed, parasite oscillations induced by the
cutoff can strongly modify the shape of the most nonlinear waves which worsen
S_k prediction. Unlike the linear method, the SNL method skillfully recovers the
wave shape with a S_k error systematically lower than 20 % with an average of
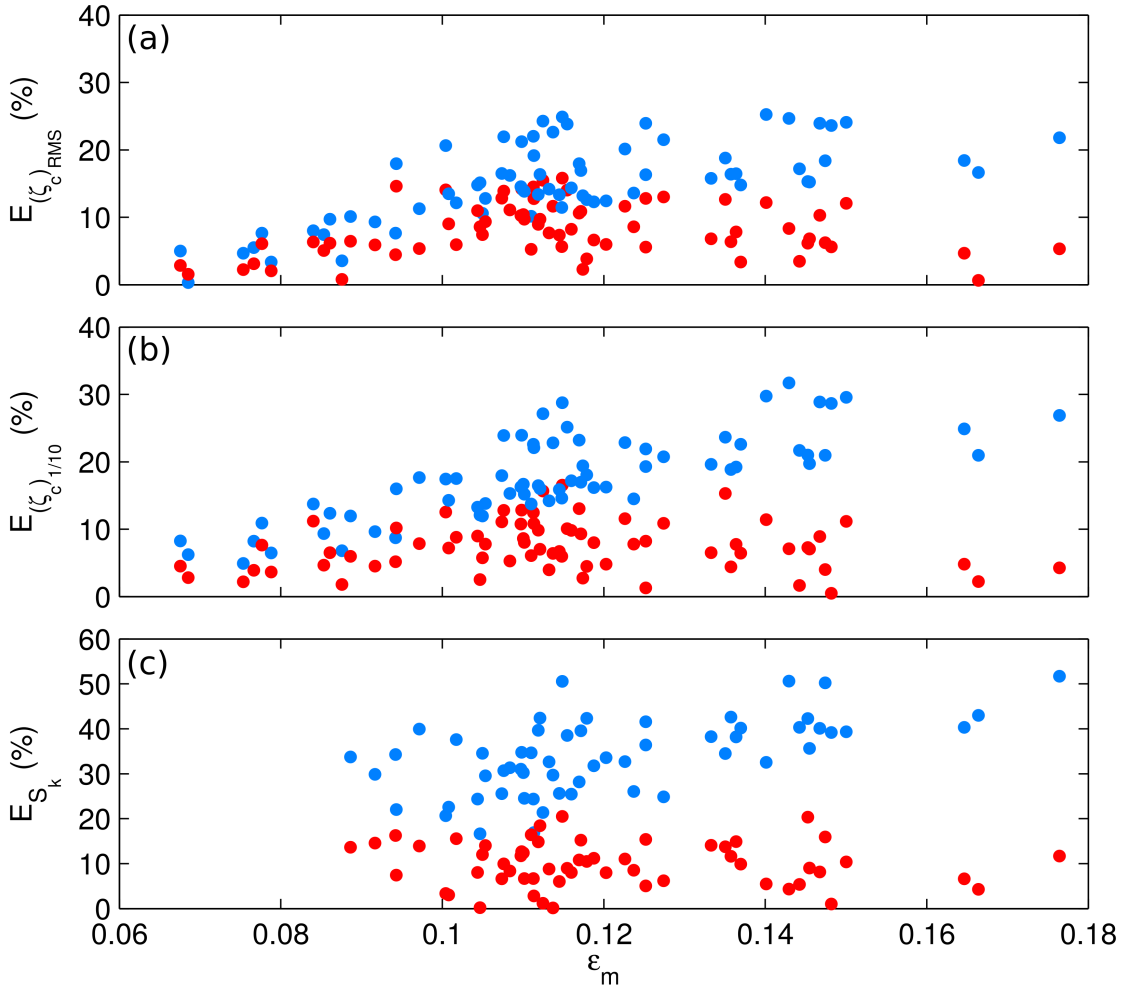8.5 %.

Figure 15: Relative error (%) of (a) the root-mean-square crest elevation $(\zeta_c)_{\mathrm{RMS}}$, (b) the average of the highest one-tenth crest elevation $(\zeta_c)_{1/10}$ and (c) the skewness parameter S_k as a function of the average nonlinear parameter ϵ_m. TFM - sharp cutoff: ζ_L (blue circles); weakly-dispersive nonlinear reconstruction: ζ_{SNL} (red circles). $f_c = 0.32$ Hz and $f_{c,\mathrm{noise}} = 1$ Hz.

Fig. 16 presents the dimensionless crest elevation of each 3560 detected individual waves for both reconstruction methods $((\epsilon_i)_L$ and $(\epsilon_i)_{\mathrm{SNL}})$ against AST measurements $((\epsilon_i)_m)$. Most of the detected waves are linear as most of $(\epsilon_i)_m$ values are relatively low (between 0.05 and 0.2). These linear waves correspond

to 78 % of the whole dataset and are well predicted by both reconstruction methods (see Fig. 16a and Fig. 16b).

However, for higher values of $(\epsilon_i)_m$ (> 0.25), the two methods show different

595 results. The linear method considerably underestimates the highest one tenth dimensionless crest elevation (average error of 20.3 %; see Fig. 16c) while the weakly-dispersive nonlinear method is able to recover the crests of the most nonlinear waves (average error of 6.9 %; see Fig. 16d). Blue crosses represent waves that meet the extreme wave criteria (Eq. 34). These extreme waves correspond

600 to 0.7 % of all detected waves and correspond to some of the most nonlinear waves of our dataset ($0.30 < (\epsilon_i)_m < 0.53$), which are correctly recovered by ζ_{SNL}, only. The linear reconstruction underestimates the dimensionless crest elevation of the detected extreme waves with an average error and a maximum error of 27.9 % and 36.6 %, respectively, against 5.4 % and 16.7 % for the SNL
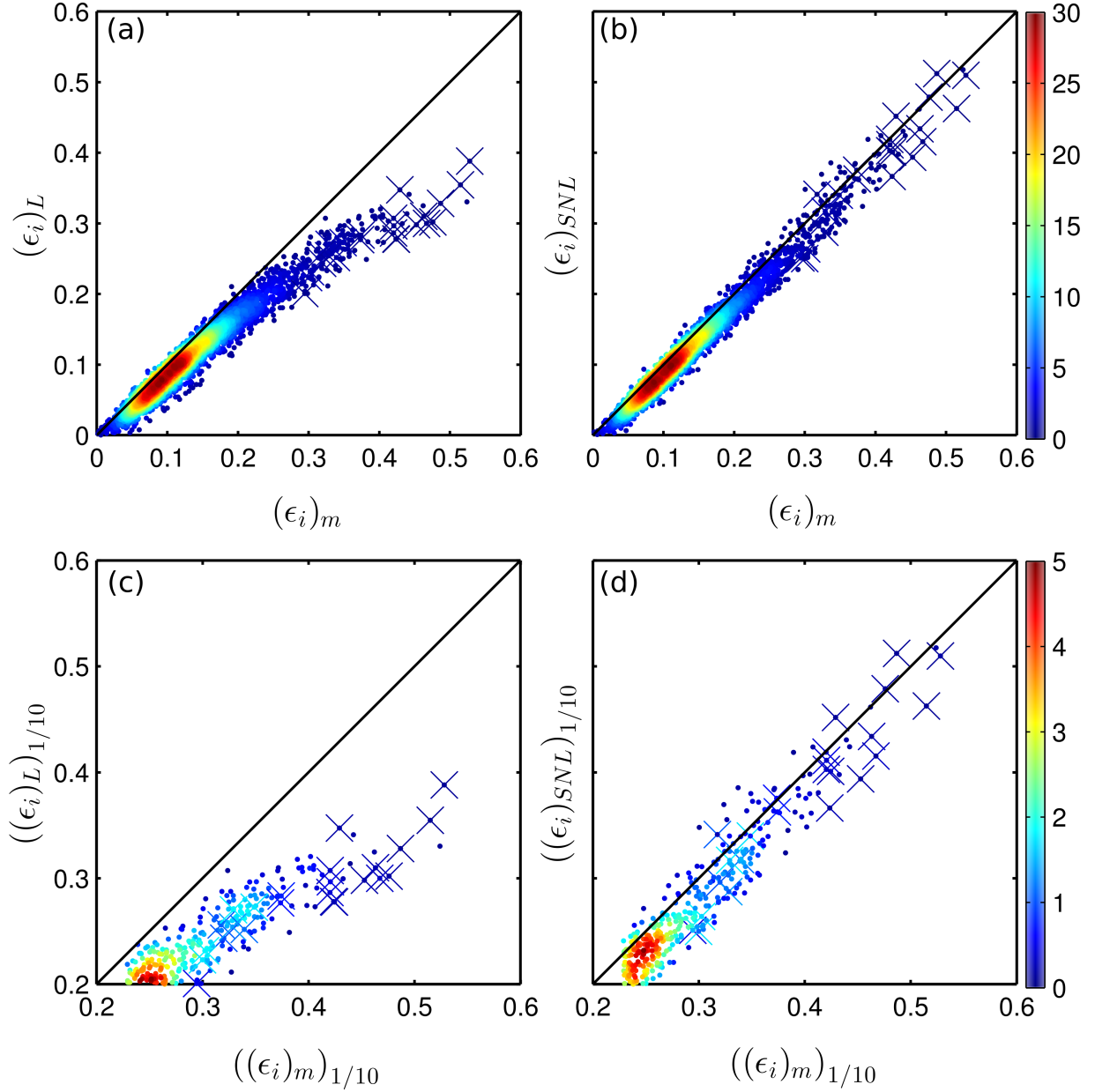
605 method.

Figure 16: Reconstructed dimensionless crest elevations versus measured crest elevations for all detected waves ((a) and (b)) and for the highest one-tenth dimensionless crest elevations ((c) and (d)). The color of each point represents its density (computed as the number of neighbooring points within a 0.015 m radius). Blue crosses show the detected extreme waves (Eq. 34). (a) and (c): TFM - sharp cutoff ζ_L. (b) and (d): weakly-dispersive nonlinear reconstruction ζ_{SNL}; see the associated equations in Tab. 1 and 2. $f_c = 0.32$ Hz and $f_{c,noise} = 1$ Hz.

41

4.3. Discussion

In the above work, the weakly-dispersive nonlinear reconstruction (ζ_{SNL} Eq. 31) was found to be essential to accurately recover the highest waves, especially in the shoaling zone. However, we have focused on weakly-dispersive waves

610 outside the surf zone ($\mu \leq 0.2$; see Fig. 6). In this way, further investigations need to be carried out to identify a threshold above which the fully-dispersive reconstruction (ζ_{NL} Eq. 29) must be used instead of the weakly-dispersive one. First findings, regarding wave data collected in laboratory experiment, seem to indicate that $\mu = 0.3$ is the transitional value above which ζ_{NL} must be used

615 instead of ζ_{SNL}. Nonetheless, evaluating this transitional value in case of *in situ* irregular waves would require additional wave data in fully-dispersive regime (i.e. waves with shorter peak periods or propagating in deeper water depth; see Fig. 17).
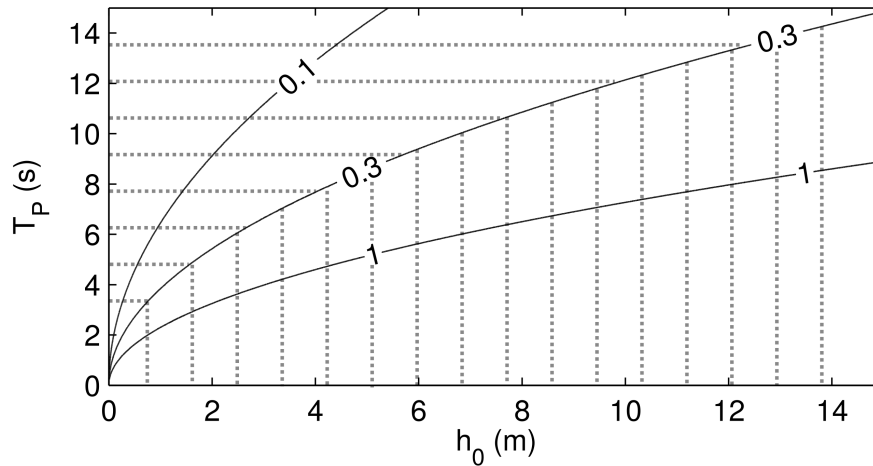

Figure 17: Shallowness parameter μ as a function of peak period T_{P} and mean water depth h_0. $\mu < 0.3$ corresponds to weakly-dispersive regime (horizontal dotted line) and $\mu > 0.3$ corresponds to fully-dispersive regime (vertical dotted line).

Although AST did not enable an accurate measurement of broken waves in our

620 experiment, it has still provided an approximate sight of the shape and crest elevation of waves inside the outer surf zone. The weakly-dispersive nonlinear

42

reconstruction was found to correctly recover such waves. Inside the inner surf zone, the sawtooth wave shape comes from the balance between the nonlinear distortion of the wave field and the turbulent dissipation within the wave front.

625 These rotational processes cannot be described with irrotational approaches. Furthermore, the pressure distribution under such waves is mainly hydrostatic (Lin and Liu, 1998 [42]). Nonlinear shallow-water equations are able to predict waves inside the inner surf zone and the swash zone as they accurately reproduce the distortion of nonlinear waves (Bonneton, 2007 [43]). Hence, the hydrostatic

630 reconstruction ($\zeta_H^{\delta_m}$ Eq. 3) would tend to be the most suitable method to recover the surface elevation of broken waves.

Concluding this section, Fig. 18 shows the range of validity of fully-dispersive, weakly-dispersive and hydrostatic reconstruction methods. An accurate direct measurement of the surface elevation of fully-dispersive waves outside the surf

635 zone and broken waves inside the surf zone is still required for identifying two thresholds: one for using ζ_{NL} or ζ_{SNL} and one for using ζ_{SNL} or $\zeta_H^{\delta_m}$ (see Fig. 18).
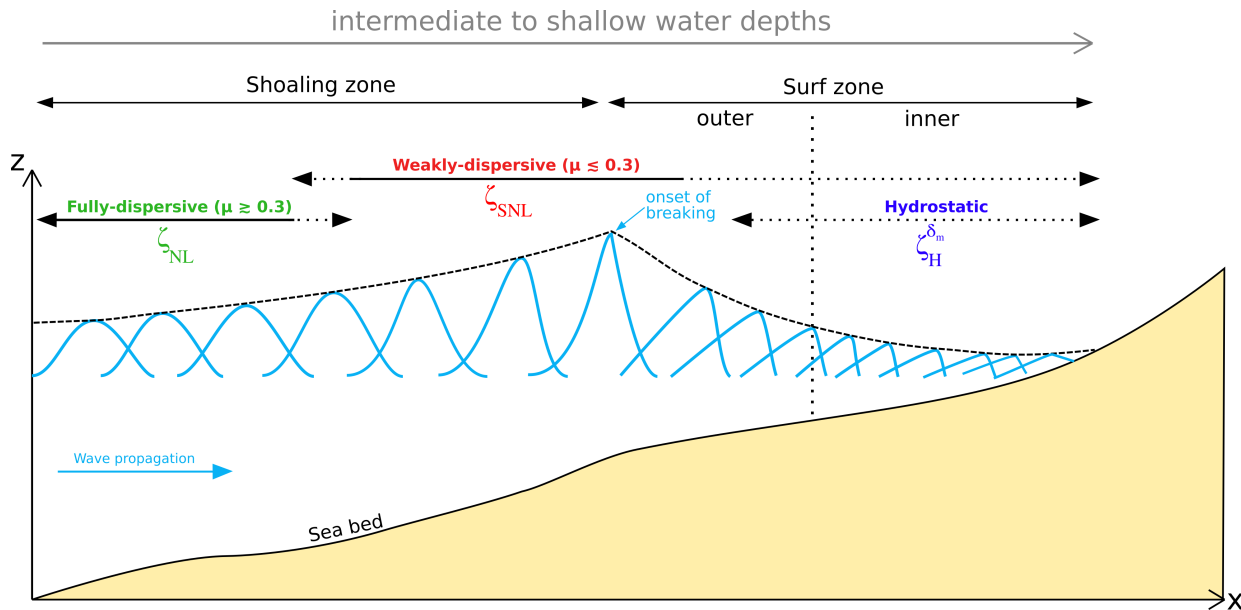
Figure 18: Range of validity of reconstruction methods. x and z are the cross-shore axis and the vertical axis, respectively. $\mu = (kh_0)^2$ is a dispersion parameter (Eq. 1).

5. Conclusion

We have applied and compared different methods to reconstruct the surface ele-
vation from pressure measurements in case of irregular weakly-dispersive waves
($\mu < 0.2$) propagating outside the surf zone ($h_0 < 4$ m). The commonly-used
transfer function method (TFM) was found to give a reliable estimate of the
significant wave height (H_{m0}) with error not exceeding 7 % in near-breaking
conditions which feature highly nonlinear waves. However, this method re-
quires the use of a cutoff frequency which restricts the reconstruction of the
most nonlinear waves. The TFM solution is very sensitive to the value of this
cutoff frequency, especially the reconstructed surface wave elevation. The latter
can be affected by the presence of parasite oscillations that strongly alter the
shape of the highest waves. Associated with the TFM, several high-frequency
tail correction procedures were tested and found to slightly improve H_{m0} predic-
tion. Nonetheless, these procedures still fail to describe the energy distribution

44

in the highest frequencies leading to an underestimation of the crest elevation of the highest wave and the skewness parameter. On the contrary, the recently developed weakly-dispersive nonlinear reconstruction method (SNL) was found to correctly reproduce the wave spectrum over a large number of harmonics which allows an accurate estimation of the peaked and skewed shape of the highest waves. More importantly, unlike the TFM, this method is able to recover the most nonlinear waves within wave groups. Some of these waves can be characterized as extreme waves and are still accurately predicted by the SNL method (average relative error of 5.4 %) compared the TFM (average relative error of 27.9 %). Well predicting these waves is essential for many coastal applications, in particular those that require a correct estimation of the highest waves such as studies on wave submersion, but also for predicting the break point position which is crucial for the calibration and the validation of wave propagation models.

6. Acknowledgements

References

[1] C. Bishop, M. Donelan, Measuring waves with pressure transducers, Coastal Engineering 11 (4) (1987) 309–328. `doi:10.1016/0378-3839(87)90031-7`.

[2] R. T. Guza, E. Thornton, Local and shoaled comparisons of sea surface elevations, pressures, and velocities, Journal of Geophysical Research 85 (C3)
(1980) 1524. `doi:10.1029/JC085iC03p01524`.

[3] D. Lee, H. Wang, Measurement of surface waves from subsurface gage, in: Coastal Engineering 1984, American Society of Civil Engineers, Houston, Texas, United States, 1985, pp. 271–286. `doi:10.1061/9780872624382.020`.

[4] P. Bonneton, D. Lannes, Recovering water wave elevation from pressure measurements, Journal of Fluid Mechanics 833 (2017) 399–429. `doi:10.1017/jfm.2017.666`.

[5] K. Martins, C. Blenkinsopp, R. Almar, J. Zang, The influence of swash-based reflection on surf zone hydrodynamics: a wave-by-wave approach, Coastal Engineering 122 (2017) 27–43. `doi:10.1016/j.coastaleng.2017.01.006`.

[6] B. Dubarbier, B. Castelle, V. Marieu, G. Ruessink, Process-based modeling of cross-shore sandbar behavior, Coastal Engineering 95 (2015) 35–50. `doi:10.1016/j.coastaleng.2014.09.004`.

[7] N. Booij, R. C. Ris, L. H. Holthuijsen, A third-generation wave model for coastal regions: 1. model description and validation, Journal of Geophysical Research: Oceans 104 (C4) (1999) 7649–7666. `doi:10.1029/98JC02622`.

[8] M. Zijlema, G. Stelling, P. Smit, Swash: An operational public domain code for simulating wave fields and rapidly varied flows in coastal waters, Coastal Engineering 58 (10) (2011) 992–1012. `doi:10.1016/j.coastaleng.2011.05.015`.

[9] P. Bonneton, F. Chazel, D. Lannes, F. Marche, M. Tissier, A splitting approach for the fully nonlinear and weakly dispersive green–naghdi model, Journal of Computational Physics 230 (4) (2011) 1479–1498. `doi:10.1016/j.jcp.2010.11.015`.

46

[10] J. Fenton, Use of the programs fourier, cnoidal and stokes for steady waves. URL http://johndfenton.com/Steady-waves

[11] J. Smith, Wave pressure gauge analysis with current, Journal of Waterway, Port, Coastal, and Ocean Engineering 128 (6) (2002) 271–275. doi:10. 1061/(ASCE)0733-950X(2002)128:6(271).

[12] J. Wolf, The analysis of bottom pressure and current data for waves, in: Seventh International Conference on Electronic Engineering in Oceanography - Technology Transfer from Research to Industry, Vol. 1997, IEE, Southampton, UK, 1997, pp. 165–172. doi:10.1049/cp:19970678.

[13] N. Jones, S. Monismith, Measuring short-period wind waves in a tidally forced environment with a subsurface pressure gauge: Measuring waves with pressure gauges, Limnology and Oceanography: Methods 5 (10) (2007) 317–327. doi:10.4319/lom.2007.5.317.

[14] B. Ruessink, K. Houwman, P. Hoekstra, The systematic contribution of transporting mechanisms to the cross-shore sediment transport in water depths of 3 to 9 m, Marine Geology 152 (4) (1998) 295–324. doi:10.1016/ S0025-3227(98)00133-9.

[15] N. Sénéchal, H. Dupuis, P. Bonneton, Preliminary hydrodynamic results of a field experiment on a barred beach, truc vert beach on october 2001, Ocean Dynamics 54 (3-4). doi:10.1007/s10236-003-0052-9.

[16] U. Neumeier, neumeier.perso.ch.

[17] P. Nielsen, Local approximations : a new way of dealing with irregular waves, 20th International Conference on Coastal Engineeringdoi:10.1061/ 9780872626003.048.

[18] J. Fenton, Polynomial approximation and water waves, in: Coastal Engineering 1986, American Society of Civil Engineers, Taipei, Taiwan, 1987, pp. 193–207. doi:10.1061/9780872626003.015.

47

[19] M. Townsend, J. Fenton, A comparison of analysis methods for wave pressure data, in: Coastal Engineering 1996, American Society of Civil ₇₃₅ Engineers, Orlando, Florida, United States, 1997, pp. 575–588. `doi:` `10.1061/9780784402429.046`.

[20] P. Nielsen, Analysis of natural waves by local approximations, Journal of Waterway, Port, Coastal, and Ocean Engineering 115 (3) (1989) 384–396. `doi:10.1061/(ASCE)0733-950X(1989)115:3(384)`.

₇₄₀ [21] B. Deconinck, K. L. Oliveras, V. Vasan, Relating the bottom pressure and the surface elevation in the water wave problem, Journal of Nonlinear Mathematical Physics 19 (sup1) (2012) 179–189. `doi:10.1142/S1402925112400141`.

[22] K. L. Oliveras, V. Vasan, B. Deconinck, D. Henderson, Recovering the ₇₄₅ water-wave profile from pressure measurements, SIAM Journal on Applied Mathematics 72 (3) (2012) 897–918. `doi:10.1137/110853285`.

[23] A. Constantin, On the recovery of solitary wave profiles from pressure measurements, Journal of Fluid Mechanics 699 (2012) 376–384. `doi:` `10.1017/jfm.2012.114`.

₇₅₀ [24] D. Clamond, A. Constantin, Recovery of steady periodic wave profiles from pressure measurements at the bed, Journal of Fluid Mechanics 714 (2013) 463–475. `doi:10.1017/jfm.2012.490`.

[25] V. Vasan, K. L. Oliveras, Water-wave profiles from pressure measurements: Extensions 68 175–180. `doi:10.1016/j.aml.2017.01.017`.

₇₅₅ [26] P. Bonneton, D. Lannes, K. Martins, H. Michallet, A nonlinear weakly dispersive method for recovering the elevation of irrotational surface waves from pressure measurements, Coastal Engineering 138 (2018) 1–8. `doi:` `10.1016/j.coastaleng.2018.04.005`.

48

[27] T. Pedersen, S. Nylund, Wave height measurements using acoustic surface tracking, in: 2004 USA-Baltic Internation Symposium, IEEE, Klaipeda, 2004, pp. 1–8. doi:10.1109/BALTIC.2004.7296806.

[28] T. Pedersen, A. Lohrmann, Possibilities and limitations of acoustic surface tracking, in: Oceans '04 MTS/IEEE Techno-Ocean '04 (IEEE Cat. No.04CH37600), Vol. 3, IEEE, Kobe, Japan, 2004, pp. 1428–1434. doi:10.1109/OCEANS.2004.1406331.

[29] K. Martins, C. Blenkinsopp, H. Power, B. Bruder, J. Puleo, E. Bergsma, High-resolution monitoring of wave transformation in the surf zone using a lidar scanner array, Coastal Engineering 128 (2017) 37–43. doi:10.1016/j.coastaleng.2017.07.007.

[30] Nortek manual : Principles of operation.
URL https://www.nortekgroup.com/manuals-quick-guides

[31] T. Pedersen, S. Nylund, A. Dolle, Wave height measurements using acoustic surface tracking, in: Oceans '02 MTS/IEEE, IEEE, Biloxi, MI, USA, 2002, pp. 1747–1754. doi:10.1109/OCEANS.2002.1191898.

[32] R. Birch, D. Fissel, K. Borg, V. Lee, D. English, The capabilities of doppler current profilers for directional wave measurements in coastal and nearshore waters, in: Oceans '04 MTS/IEEE Techno-Ocean '04 (IEEE Cat. No.04CH37600), Vol. 3, IEEE, Kobe, Japan, 2004, pp. 1418–1427. doi:10.1109/OCEANS.2004.1406330.

[33] H. E. Power, M. G. Hughes, T. Aagaard, T. E. Baldock, Nearshore wave height variation in unsaturated surf, Journal of Geophysical Research 115 (C8). doi:10.1029/2009JC005758.

[34] H. Power, M. Hughes, T. Baldock, A novel method for tracking individual waves in the surf zone, Coastal Engineering 98 (2015) 26–30. doi:10.1016/j.coastaleng.2015.01.006.

49

[35] M. S. Longuet-Higgins, R. W. Stewart, Radiation stress and mass transport in gravity waves, with application to 'surf beats', Journal of Fluid Mechanics 13 (04) (1962) 481. doi:10.1017/S0022112062000877.

[36] G. Symonds, D. Huntley, A. Bowen, Two-dimensional surf beat: Long wave generation by a time-varying breakpoint, Journal of Geophysical Research 87 (C1) (1982) 492. doi:10.1029/JC087iC01p00492.

[37] D. Roelvink, A. Reniers, A. van Dongeren, J. van Thiel de Vries, R. McCall, J. Lescinski, Modelling storm impacts on beaches, dunes and barrier islands, Coastal Engineering 56 (11-12) (2009) 1133–1152. doi:10.1016/j.coastaleng.2009.08.006.

[38] J. Baumann, E. Chaumillon, X. Bertin, S. J., B. Guillot, M. Schmutz, Importance of infragravity waves for the generation of washover deposits, Marine Geologydoi:10.1016/j.margeo.2017.07.013.

[39] X. Bertin, A. de Bakker, A. van Dongeren, G. Coco, G. André, F. Ardhuin, P. Bonneton, F. Bouchette, B. Castelle, W. C. Crawford, M. Davidson, M. Deen, G. Dodet, T. Guérin, K. Inch, F. Leckler, R. McCall, H. Muller, M. Olabarrieta, D. Roelvink, G. Ruessink, D. Sous, E. Stutzmann, M. Tissier, Infragravity waves: From driving mechanisms to impacts, Earth-Science Reviews 177 (2018) 774–799. doi:10.1016/j.earscirev.2018.01.002.

[40] J. Battjes, H. Bakkenes, T. Janssen, A. van Dongeren, Shoaling of subharmonic gravity waves, Journal of geophysical researchdoi:10.1029/2003JC001863.

[41] K. Dysthe, H. Krogstad, P. Müller, Oceanic rogue waves, Annual Review of Fluid Mechanics 40 (1) (2008) 287–310. doi:10.1146/annurev.fluid.40.111406.102203.

[42] P. Lin, P.-F. Liu, A numerical study of breaking waves in the surf

zone, Journal of Fluid Mechanics 359 (1998) 239–264. `doi:10.1017/S002211209700846X`.

815 [43] P. Bonneton, Modelling of periodic wave transformation in the inner surf zone, Ocean Engineering 34 (10) (2007) 1459–1471. `doi:10.1016/j.oceaneng.2006.09.002`.